Construction and subduction of the Louisville Ridge, SW Pacific – insights from wide-angle seismic data modelling

Authors: Robinson, A.H.[1], Peirce, C.[1] and Funnell, M.J.[1]

[1] Department of Earth Sciences, Durham University, South Road, Durham, DH1 3LE, UK.

Accepted Received in original form

Abbreviated title: Construction and subduction of the Louisville Ridge

Corresponding author:
Adam Robinson
Department of Earth Sciences
Durham University
DH1 3LE
Durham
United Kingdom
Email: a.h.robinson@durham.ac.uk

SUMMARY

The Louisville Ridge is a c. 4000 km-long chain of seamounts in the SW Pacific that is currently being subducted at the Tonga-Kermadec trench. The Pacific plate, on which the chain sits, is subducting obliquely beneath the Indo-Australian plate. Combined with the oblique strike of the chain relative to the margin, this results in the southward migration of the ridge-trench intersection and leads to significant along-trench variation in forearc morphology as a result of tectonic erosion processes. To understand how the subduction of such large-scale plate topography controls forearc deformation, knowledge of the structure of the seamounts themselves and the crust upon which they lie, and how these seamounts are deformed prior to and on entering the trench is required. The *TOTAL* (*To*nga *T*hrust earthquake *A*sperity at *L*ouisville Ridge) project aimed to address these questions by undertaking a multi-disciplinary geophysical study of the ridge-trench intersection and surrounding region, as part of which multichannel and wide-angle seismic, gravity, and swath bathymetry data were acquired along a ~750 km-long profile extending along the Louisville Ridge and into the adjacent Tonga forearc.

We show that each of the largest, single edifice seamounts (called Osbourn and 27.6°S) imaged has a discrete core of elevated seismic velocity ($V_p \geq 6.0$ km s^{-1}) and density (2600 kg m^{-3}) relative to the adjacent Pacific oceanic crust, reaching to within 1.0-1.5 km of the seabed at their summits. However, there is no evidence of significant crustal thickening associated with individual seamounts, or that the crust beneath the Louisville Ridge Seamount Chain as a whole is significantly thicker than the surrounding oceanic crust of the Pacific plate.

Despite significant forearc deformation, we find no evidence to suggest that the most recent seamount of the Louisville Ridge to have been subducted, was subducted intact. The degree of plate bend-related faulting being experienced by the next seamount to subduct (Osbourn) suggests that they may instead be disarticulated to a size smaller than the imaging resolution in the trench region. In addition, distinguishing between seamount flank and intra-seamount saddle material based on seismic velocity alone is not possible. Therefore, determining how, and where, already subducted seamounts are located beneath the forearc of the overriding plate is entirely dependent on imaging any high velocity core, and that core having remained relatively intact.

Key words: controlled source seismology, crustal structure, oceanic hotspots and intraplate volcanism, subduction zone processes.

1. INTRODUCTION

Seamount chains represent a record of the modification of the oceanic crust by intrusive and extrusive magmatic processes, including hotspot magmatism (e.g. Wilson 1963; Morgan 1971), small-scale mantle convection (e.g. Ballmer et al. 2007), and localised lithospheric extension (e.g. Sandwell et al. 1995). Geophysical studies reveal diversity in seamount crustal and upper mantle structures associated with these processes (e.g. Watts et al. 1985; Caress et al. 1995: Kaneda et al. 2010; among others), with an apparent correlation between the seamount crustal structure and the age of the oceanic lithosphere at the time of volcanism (e.g. Pollack et al. 1981).

Seamounts also represent significant plate topography, and when subducted it is likely that they affect inter-plate boundary processes (e.g. Rosenbaum & Mo 2011), inducing along-strike variation in trench and forearc morphology (e.g. Kopp 2013), seismicity (e.g. Habermann et al. 1986) and arc volcanism (e.g. McGeary et al. 1985). During subduction the seamounts themselves may become decapitated (Cloos 1992; Cloos & Shreve 1996) or disaggregated by faulting, and deform the overriding forearc orthogonal to the trench (e.g. Lallemand et al. 1992). In order to better understand the formation and structure of a seamount chain and its interaction with a trench system upon subduction, a structural model of the ridge-trench intersection is required.

The *TOTAL* (*To*nga *T*hrust earthquake *A*sperity at *L*ouisville Ridge – Grevemeyer & Flueh 2008; Peirce & Watts, 2011) project aimed to address these questions by undertaking a multi-disciplinary geophysical study of the Louisville Ridge-Tonga-Kermadec trench intersection and surrounding region in the SW Pacific. In this paper, we present new wide-angle and multichannel seismic data that image the Louisville Ridge Seamount Chain (LRSC) and Tonga forearc along strike of the seamount chain. These data are synthesised with other models from the *TOTAL* project (e.g. Contreras-Reyes et al. 2010, 2011; Stratford et al. 2015; Funnell et al. 2017) in order to: i) characterise the crust and upper mantle structure for ~500 km from the Tonga-Kermadec trench-LRSC intersection, particularly focussing on the next adjacent seamounts along the LRSC (Canopus and 27.6°S seamounts) that are, as yet, unaffected by plate bend-related faulting; ii) constrain variation in the crustal structure and deformation of Osbourn seamount as a result of subduction of the Pacific plate; and iii) follow the projected strike of the LRSC into the subduction zone and across the overriding forearc, to better understand how such seamounts may be affected by plate boundary processes. Finally, we critically appraise our model to determine the scale of feature that can be reliably resolved, as a control on the limit to which features of our model can be interpreted.

2. TECTONIC SETTING

Subduction initiated at the Tonga-Kermadec trench (TKT) in the Eocene (~52 Ma – Meffre et al. 2012) with the margin currently demonstrating some of the highest convergence rates in the global subduction system (240 mm yr^{-1} – von Huene & Scholl 1991; DeMets et al. 2010), exhibiting a linear trench-arc structure, and being characterised by a complex series of arcs and backarc basins (Ruellan et al. 2003).

The Louisville Ridge Seamount Chain currently intersects the trench at ~25.8°S and separates the Tonga trench and forearc to the north from the Kermadec trench and forearc to the south (Fig. 1 – Lonsdale 1986; Ballance et al. 1989).

The LRSC is an approximately 4000 km-long, broadly NW-SE trending chain of Cretaceous-Cenozoic seamounts and guyots (Fig. 1a). The oldest seamounts are located on oceanic lithosphere which was accreted at the Osbourn Trough (Fig. 1b); a palaeo-spreading centre that is thought to be related to the rifting of the Hikurangi and Manihiki Plateaux (Downey et al. 2007). Magnetic anomaly patterns provide limited constraint on the actual age of initiation and cessation of spreading, since the crust in the vicinity of the LRSC-TKT intersection was accreted during the Cretaceous Normal Superchron (Cande & Kent 1992). However, dated dredge samples do provide some constraint, to the period ~121 Ma (Beier et al. 2011) to 83-71 Ma (Billen & Stock 2000), and indicate an intermediate-to-fast spreading rate.

The oldest extant seamount, Osbourn, has an $^{40}Ar/^{39}Ar$ age of between 76.7 ± 0.8 Ma and 78.8 ± 1.3 Ma (Koppers et al. 2004). This seamount intersects the TKT at ~25.8°S (Fig. 1b), and is currently being deformed by plate bend-related normal faults (Fig. 2). The LRSC as a whole exhibits age progression along-chain, although this is not always a linear increase in age with distance (Koppers et al. 2004; 2011), and little overall chemical and isotopic variation along its length (Beier et al. 2011; Nichols et al. 2014).

As the strike of the LRSC and direction of Pacific plate motion are both oblique to the plate boundary, the intersection point is migrating southwards at 120-180 mm yr^{-1} (Fig. 1b – Lonsdale et al. 1986; Ballance et al. 1989), resulting in along-margin variability in structure of the trench (e.g. Clift et al. 1998), forearc (Clift & MacLeod 1999), arc (England et al. 2004), and back-arc (Bevis et al. 1995). The LRSC-TKT intersection is also marked by an ~200 km-wide zone of seismic quiescence (Scholz & Small 1997). However, the location of this zone is offset to the south from the point of the intersection (Timm et al. 2013).

Consequently, the observed along-strike morphology of the forearc and trench directly attributed to LRSC subduction has resulted a number of theories related to where collision started to the north, and where is and what remains of the Louisville Ridge that has subducted to date. Ruellan et al. (2003), Bonnardot et al. (2007) and Stratford et al. (2015) suggest or assume that the LRSC extends linearly following its current bathymetric trend into the subduction zone, while Timm et al. (2013) and Bassett & Watts (2015) propose that a westward bend of up to 35° in the strike of the chain occurs at the current ridge-trench intersection point. The location of initiation of LRSC subduction adds further uncertainty, with Ruellan et al. (2003) and Bonnardot et al. (2007) proposing the northern end of the subduction zone at ~16°S, while others (e.g. von Huene & Scholl 1991; Lallemand et al. 1992; Wright et al. 2000; Contreras-Reyes et al. 2011; Stratford et al. 2015) suggest to the north of Horizon Deep Bight at ~22.5°S, where the Tonga trench exhibits an ~80 km arcward offset (Fig. 1). These contrasting theories imply that not only are there significant gaps in our understanding of LRSC itself, but also how it enters

the trench and what its fate is throughout subduction.

3. DATA ACQUISITION

The *TOTAL* project comprised two research cruises aboard the R/V Sonne, namely SO195 (Grevemeyer & Flueh 2008) and SO215 (Peirce & Watts 2011), during which a series of multichannel seismic (MCS) reflection and wide-angle (WA) seismic refraction profiles was acquired (Fig. 1b), together with multibeam swath bathymetry (using a Kongsberg Simrad EM120 multibeam echosounder) and gravity data (using a Lacoste & Romberg air-sea gravimeter from the UK's National Marine Equipment Pool). In addition, a number of measurements of water column properties were made using a sound velocity probe (SVP) and expendable bathymetric thermographs (XBT). In this paper we present the results of modelling data acquired along Profile C during SO215, and discuss our model in the context of Profiles A (Stratford et al. 2015) and B (Funnell et al. 2017) also from SO215, and Profiles P02 (Contreras-Reyes et al. 2011) and P03 (Contreras-Reyes et al. 2010) from SO195, all of which intersect it, to provide a three-dimensional perspective.

Profile C is an ~750 km-long coincident MCS-WA profile (Fig. 3) that traverses the LRSC, crossing the 27.6°S, Canopus and Osbourn seamounts, before extending along LSRC-strike into the forearc of the overriding Indo-Australian plate. This seismic profile was acquired using a 5440 in^3 (89.15 l), 12 Sercel G-gun airgun array, towed at 7.5 m depth. MCS data were recorded by a 240 channel, 3000 m multichannel streamer with 12.5 m active group length, towed at 10 m depth. Shot gathers were recorded at a sampling rate of 2 ms and trace length of 29 s, with shots fired at 60 s intervals which, at 4.5 kn survey speed, resulted in a shot spacing of ~150 m.

The WA seismic data were recorded contemporaneously using an array of 52 ocean-bottom seismographs (OBSs); 42 of the LC-type from the UK Ocean-Bottom Instrumentation Facility (OBIF) and 10 KUM 'deep-water' type from IFM-Geomar. Each instrument was fitted with a hydrophone and three-component geophone package, and data were recorded at sampling rates of 250 Hz and 200 Hz for the OBIF and IFM-Geomar instruments respectively.

4. MCS DATA PROCESSING

The MCS data were acquired along Profile C primarily to estimate the thickness of any sediment cover to inform the starting point for WA data forward modelling. As both MCS and WA seismic data were acquired contemporaneously, a compromise had to be made between the firing rate and its consequence for water wave wrap-around in the WA data, that resulted in a relatively low fold (~10) MCS data set. Coupled with the highly variable seabed topography and complex subsurface geological features, the resulting gathers had a relatively poor signal-to-noise ratio (SNR). Sorting to 25 m common mid-point (CMP) super-bins increased the fold by a factor of ~4, and improved the post-stack SNR and vertical resolution of the intra-sediment reflectivity significantly, without compromising horizontal resolution,

as the characteristic lateral scales of seabed features and imaging targets were still significantly larger than the bin size.

As the aim of the initial MCS data processing was to enable location and thickness measurement of any observed sediment cover, a simple processing flow was adopted that included zero-phase Butterworth band-pass filtering (3-10-100-120 Hz) of the CMP sorted data to remove swell noise, NMO correction using a simple outline velocity model derived by velocity analysis in regions where the basement is covered by sediment, and then stacking. In the upper forearc region, both brute and velocity analysis-derived stacking resulted in the appearance of artefacts in the stacked section, in the form of steeply dipping, high amplitude events and significant vertical smearing of reflector events respectively. Inspection of unstacked, sorted CMP gathers indicated the source of these artefacts was in the far-offset channels, and to be most likely related to reverberating signals in the water column. A mute was designed and applied to the data in this region, which successfully removed these artefacts. Simple post-stack statistical Wiener deconvolution was further applied to reduce source signal reverberation. A Kirchhoff post-stack time migration at 1.5 km s^{-1} was then applied to reduce seabed scatter and diffractions that obscured the sediment reflectivity, particularly in highly faulted regions. Finally, a cosmetic top mute was applied to remove water column noise for display purposes.

The two-way travel-time (TWTT) of the base-sediment reflector was then picked (Fig. 3b) and converted to depth using an average velocity of 2.0-2.5 km s^{-1}. Following WA seismic data modelling, the MCS data were restacked using a more detailed velocity model informed by the WA velocity-depth model. The final-form MCS section will, therefore, be discussed in Section 7.5 in the context of the results of WA seismic data modelling.

5. WA DATA TRAVEL-TIME PICKING

Lateral variations in geological structure and seabed topography generally control the SNR and the characteristics of seismic phases recorded by each instrument. Wherever possible the travel-time picks were made using unfiltered hydrophone data, although for some OBSs application of a low cut, 1-2 Hz minimum-phase filter was necessary to remove low frequency water column noise. Picks were assigned to one of the following phase types, based on the offset and apparent velocity of each arrival:

1) P_w - water wave direct arrival;
2) P_{wm} - water wave first multiple;
3) P_s - sediment refracted arrival;
4) P_g - crustal refracted arrival;
5) P_mP - Moho reflection; and
6) P_n - mantle refracted arrival.

Example record sections, displaying picked arrivals for OBSs located along the Louisville Ridge (C04, C20), at the ridge-trench intersection (C41) and on the forearc of the overriding plate (C53), are shown in Figs 4-7, respectively. Pick uncertainties, summarised in Table 1, were calculated for each OBS and

primarily defined by phase assignment, SNR and shot-receiver offset. Instruments located at and around the ridge-trench intersection had particularly large uncertainties due to greater instrument location error resulting from the extreme water depth and strong water column current, in addition to particularly low SNR resulting from the rugged seabed topography.

6. WA DATA FORWARD MODELLING

Forward ray tracing, using *rayinvr* (Zelt & Smith 1992), was chosen as the primary velocity modelling technique for the WA seismic dataset because of the significant seabed topography, the profile bend, and the degree of lateral heterogeneity anticipated in crustal structure. Profile C OBS locations, shot points, and bathymetry data were projected from geographic coordinates into distance along profile, hereafter abbreviated to d.a.p., and by dividing the profile into two segments of ~500 km and ~225 km in length with a junction located at 27.59°S 174.20°W, matching the bend in the LRSC trend at this point (Fig. 3a).

6.1 Forward model initialisation

The forward velocity-depth model was initialised with a water column layer thickness defined by the seabed depth along profile, sampled from the swath bathymetry data. A model node spacing of ~750 m was chosen as this sufficiently replicated the longer wavelength variation to within the resolution of the WA seismic data and modelling approach without oversampling. OBS locations were constrained within the model space by first inspecting the direct water wave arrivals to find the zero-offset shot location and corresponding seabed depth, and then by ray-trace modelling the water wave arrival travel-time picks through a water column layer initially assigned a P-wave velocity of 1.5 km s^{-1}. The water column velocity structure was then further iteratively refined (using XBT measurements along profile as a starting point), together with OBS locations and depths, until a good fit between modelled and observed water waves was achieved ($\chi^2 = 1.11$; Table 1).

The top of the oceanic basement was added using the depth-converted base-sediment interface picked from the MCS record section (Fig. 3b – Section 4), sampled to a variable node spacing of between 0.75 and ~2 km to faithfully reproduce the lateral variability. Below this, a standard oceanic crustal velocity-depth structure (after White et al. 1992) was constructed using laterally continuous layers, hence the initial model did not initially include a representation of the plate boundary. From 0.75 km at the seabed, the horizontal node spacing of the starting model increased to a maximum of 20 km at Moho depth.

6.2 Modelling approach

Wide-angle seismic data modelling was conducted using a top-down approach, with rays traced for all crustal phases in the positive (southeast) and negative (northwest) along-model directions from each OBS to appraise arrival phase assignment in the first instance. As modelling progressed by iteratively

adjusting model layer interface depths and velocities, it became clear that the observed travel times could not be matched without introducing a representation of the down-going plate. Consequently, the SLAB1.0 global model (Hayes et al. 2012) was used to provide initial constraint on the location and dip of the plate boundary at depth below seabed.

In order to resolve the velocity structure beneath 27.6°S seamount (Fig. 3), it was necessary to trace rays from shots to the north of the profile bend into instruments to the south, and vice versa. Since these propagation paths would have an out-of-plane component, only shot-receiver pairs that minimized the associated error due to a difference in travel time, τ, to within acceptable limits were selected. These limits were defined to be an addition of up to 50% and 100% of the existing P_g and P_n pick uncertainties respectively ($\tau_{max(Pg)}$ = 35 ms and $\tau_{max(Pn)}$ = 100 ms), and were incorporated into the travel-time pick errors for the relevant phases of the shot-OBS pairs used to ray-trace this part of the model. Shot-receiver pairs were selected using the condition that the direct ray paths (across-the-corner) must sample approximately the same velocity structure as they would if travelling along the trend of Profile C (around-the-bend).

The fit of modelled to observed travel-time picks was assessed using the root-mean-square travel-time residual (T_{rms}), and the normalized chi-squared statistic (χ^2), the latter of which considers the pick uncertainties. A $\chi^2 = 1$ represents a fit with the model error equivalent to the pick uncertainty; values of $\chi^2 < 1$ represent an over-fit. The final velocity-depth model (Fig. 8 – henceforth referred to as the *forward model*) is based on a fit to 60,736 travel-time picks and has an overall $\chi^2 = 2.45$ and T_{rms} = 145 ms (Table 1). The oceanic crust of each of the down-going and overriding plates comprises three layers, with the upper and middle layer separated by a first-order velocity discontinuity (step in velocity), and the middle and lower crust separated by a second-order discontinuity (change in gradient). The features of this model are discussed in Section 8.

7. ROBUSTNESS OF THE FORWARD MODEL

7.1 Modeller bias and uniqueness

Inversion modelling of the travel-time picks was conducted using *FAST* (Zelt & Barton 1998) to test the degree of modeller bias and uniqueness of the forward model. The *FAST* inversion algorithm performs iterative updates to a smooth velocity field, averaging the seismic velocity structure along ray paths, and aims to minimise travel time residuals in order to reduce the χ^2 fit to 1. As only the first-arriving phase for any shot-receiver pair can be used in the inversion, this reduced the total number of travel-time picks used to 49,779.

The initial starting model was parameterised on a 0.2 x 0.2 km uniform grid with a two-gradient velocity profile draped beneath the bathymetry, comprising V_p = 2.5-6.0 km s^{-1} from the seabed to 1.5 km depth below seabed (b.s.b.), and V_p = 6.0-7.5 km s^{-1} from 1.5 km b.s.b. to 16 km depth below sea surface (b.s.s.; Fig. 9a). Below 16 km b.s.s., the velocity was set to 7.5 km s^{-1}. At 22 km b.s.s., below

the maximum depth of any ray-trace forward-modelled turning rays, the velocity was fixed at 8.0 km s^{-1} throughout inversion modelling to prevent high velocity upwards smear through the model space. This bounding contributes to the apparent generation of a velocity inversion artefact at the base of the region of ray coverage.

Running the inversion over eight iterations at 8 x 3 km inverse cell size followed by five iterations at 4 x 2 km inverse cell size, produced a velocity-depth model (Fig. 9b – henceforth referred to as the *inverse model*) with T_{rms} = 129 ms and χ^2 = 2.29. The *inverse model* agrees with the *forward model* to ± <0.2 km s^{-1} throughout the majority of the crust, where both are sampled by rays (Figs 9c & 8b respectively). Greater mismatches, of up to ± <0.5 km s^{-1} are associated with first-order velocity discontinuities located at the summits of the seamount internal cores, around the down-going plate interface and at the base of the crust, due to the inherent smoothing associated with the inversion modelling approach applied. That both the forward and modeller-independent inversion modelling approaches used in this study result in similar models suggests that the *forward model* is a significant result and, thus, indicates the robustness of the features shown by both modelling approaches (Zelt et al. 2003).

7.2 Model resolution

To determine the minimum resolvable feature size, model resolution testing was performed on the *inverse model* using a checkerboard approach (Zelt 1998; 1999). The *inverse model* was first convolved with a regular checkerboard of alternating polarity velocity anomalies with a velocity perturbation of ±5% relative to the background model value (Fig. 10b,c), and synthetic travel times were generated by forward finite difference ray-tracing through this perturbed model. Gaussian noise was then added to the resultant travel times based on the assigned pick uncertainties. These synthetic travel times were then inverted using the same parameters as before, with the process repeated for a range of checkerboard patterns. The tested checkerboard patterns covered a broad range of cell sizes, and include the application of lateral and vertical shifts to the input pattern of 0.5, 1.0 and 1.5 times the anomaly width and depth in order to test the sensitivity to checkerboard cell edge coincidence with large bathymetric contrasts.

Overall, good checkerboard recovery was achieved throughout the crust and into the upper mantle for the 20 x 4 km (horizontal x vertical) and 30 x 4 km input anomaly sizes (Fig. 10h,i), apart from two regions of limited ray coverage (cf. Fig. 9c), those being the forearc and down-going plate regions immediately adjacent to the trench, and beneath the profile bend at 27.6°S. Recovery is good in well-sampled locations shallower than 12 km depth for the 15 x 4 km checkerboard (Fig. 10g), implying a generally higher resolution in that part of the model. At and below 3 km vertical anomaly size, good recovery is limited to only the very uppermost part of the crust (Fig. 10d-f). Thus, for a typical-sized LRSC seamount – a summit diameter of 20-30 km, basal diameter of 40-60 km, prominence above the

seafloor of 3-4 km, and total crustal thickness of up to 10 km – the results of checkerboard testing indicate that seamount-sized velocity anomalies should be recoverable throughout the model.

7.3 Model sensitivity

To test the *forward model* for its sensitivity to changes in velocity and depth, perturbations to this model were applied, the model re-traced and the fit reappraised. For the overriding and down-going plates respectively, we chose threshold fit values of χ^2>3.0 and χ^2>3.6, which represent an ~20% increase in the T_{rms}, as cut-offs for defining when the model misfit became unacceptable. Four types of perturbation were applied to the *forward model* by adjusting the:

i. layer interface depth, defined here to be that at the top of a layer;
ii. velocity at the top of a layer;
iii. velocity at the base of a layer; and
iv. bulk velocity of a layer whilst keeping the velocity gradient the same.

The presence of the second-order velocity discontinuity between the middle and lower crustal layers of each plate was preserved throughout the testing procedure. In the case of the bulk velocity test, this means that a perturbation to one of the two layers also has an impact on the velocity gradient of the other, and so these tests cannot be truly independent. In addition, the top and base velocity tests for the layers directly above and below the second-order discontinuity are, by definition, complementary in their effect.

Parts of the *forward model* representing the Pacific and Indo-Australian plates were also independently tested by separately only tracing ray groups for instruments located on each plate, such that the fit statistic is not unduly biased by rays being traced through unperturbed parts of the model. In the case of the trench-proximal instruments, this required including the travel time picks for these instruments in the tests for both plates.

The overriding Indo-Australian plate has decreasing sensitivity to layer interface depth with increasing depth below seabed, from ± 0.4 km in the middle crust to between +0.9 and -1.4 km (negative = shallower) at the Moho. The down-going Pacific plate has a generally similar sensitivity to layer interface perturbations in the middle crust (+0.5/-0.2 km), but better constraint on Moho depth (+0.2/-0.6 km). Analysis of P_n arrival frequency spectra suggests that the dominant signal frequency band expected for phases travelling from the base of the crust and uppermost mantle is a few-to-15 Hz, corresponding to wavelengths of >0.5 km. Therefore, the best-to-be-expected resolution for an interface at Moho depth is 0.125 km, which is small compared to the corresponding modelled depth confidence limits. This indicates that model sensitivity at the base of the crust is influenced primarily by a lack of rays sampling the mantle beneath both plates, and by the size of the P_n pick uncertainties. Overall, this conclusion suggests that the model is least well constrained in these regions.

Velocity sensitivity is generally uniform throughout the oceanic crust of the entire model at better than ± 0.4 km s^{-1}. The exception to this is the uppermost crustal layer of the Pacific plate, which appears

to accommodate much larger increases in layer velocity before a misfit is achieved. This may simply be a result of significant lateral heterogeneity within this layer being compensated differentially as the perturbations are applied and, thus, may indicate that homogeneous sensitivity testing may not be the optimal approach for this layer, although it is sufficient to be indicative for interpretation purposes.

The results of sensitivity testing are summarised in Table 2. Consequently, for the remainder of this paper, layer thicknesses and velocities determined from the *forward model* will be quoted with the relevant sensitivity to indicate their degree of confidence.

7.4 Gravity modelling as an independent test of uniqueness

An independent check on model uniqueness can be achieved by comparing the observed ship-measured free-air anomaly (FAA) with that calculated having converted the *forward model* to a density-depth model (henceforth known as the *density model*). *Density model* block geometries were determined from *forward model* velocity contours representing principal crustal layer interfaces, with water and sediment blocks extending along the entire profile. A distinct set of crustal and upper mantle blocks were defined for each plate. The density model was extended to 100 km depth using SLAB1.0 (Hayes et al. 2012) to constrain the location of the down-going plate, and to 1000 km laterally from the north-western and south-eastern ends to prevent edge effects. Each model block was assigned a density based on its average velocity, using the standard velocity-density relationships of Nafe & Drake (1957), Kuo & Forsyth (1988) and Carlson & Herrick (1990).

Calculation of the FAA was performed in two dimensions using *grav2d*, based on the method of Talwani et al. (1959). As gravity modelling is not being conducted independently, only as a test that the forward model velocity-derived density model does not produce a gravity anomaly that is significantly different from that which is measured, this assumption is acceptable. Without adjustment of any layer interface geometry in regions well constrained in the *forward model*, the *density model* produces a gravity anomaly that fits the observed FAA with an RMS residual of 73.3 mGal (Fig. 11, blue line). An improved fit (15.7 mGal; green line) is achieved by assigning different densities to the uppermost mantle beneath each plate, which can be reconciled since these regions have little-to-no constraint based on the WA seismic modelling alone. The best-fit (14.0 mGal; red line) was achieved by making further minor alterations, which can be accommodated within the *forward model* sensitivity, to block geometries and/or densities in the least well constrained crust beneath the lower slopes of the forearc adjacent to the trench. A misfit remains, however, particularly so between the trench and Osbourn seamount (200-275 km d.a.p.) and in the mid-slope region of the forearc (25-100 km d.a.p.) which will be discussed in Section 8.3.

7.5 MCS reflection data restacking

As a final uniqueness check, the *forward model* was converted to a stacking velocity-TWTT model using an inverse-Dix (Dix 1955) approach, and the result used to restack the MCS data. Examples of

the improvement in reflectivity achieved using this enhanced stacking velocity model are shown in Fig. 12, processed using the same migration and display parameters used initially.

Improved MCS reflectivity is most apparent in the saddles between seamounts (Figs 12e,f), in regions <2 s TWTT below the seabed, and where V_p is less than 6 km s^{-1}. Reflectors here are irregular and continuous only over length scales of 10-20 km. Stack improvement is limited in the forearc of the overriding plate, although there is some suppression of the interference caused by the water column multiple in the uppermost forearc between 0-50 km and 1.5-3.0 s TWTT (Fig. 12b). Overall, restacking does not appear to improve imaging of deeper crustal features such as the Moho. It is more likely that the poor imaging at greater depths is a direct result of the complex bathymetry and subsurface geology significantly scattering the down-going wave-field.

7.6 A robust solution

All of the dependent and independent approaches used to test the *forward model* for robustness and modeller bias produce consistent results and fits to their respective datasets to within the associated uncertainties. As such, the *forward model* may be regarded as a robust, well-constrained representation of the sub-surface geological structure of the Louisville Ridge and Tonga forearc traversed by Profile C. This model will now be interpreted and then set in the context of the other intersecting velocity-depth profiles acquired as part of the *TOTAL* project.

8. MODEL INTERPRETATION

8.1 Background Pacific plate

Profile C traverses only a short length of background Pacific oceanic crust unmodified by magmatic eruption or intrusion associated with seamount formation (Fig. 8; 690-726 km d.a.p.) and, therefore, the observations that can be made are limited. A thin sedimentary cover (~400 m) with V_p = 2.3-2.6 (± 0.1) km s^{-1} overlies a topmost crustal layer <0.5 (+0.2/-0.1) km-thick with V_p = 3.5-5.0 (± <0.4) km s^{-1}. Below this, the middle crust layer thickness varies from 1.5 km close to the LRSC to 1.0 (± 0.4) km at the southernmost end of the profile, and velocity increases from 5.0 (+0.4/-0.3) km s^{-1} at the top to ~6.5 (± 0.2) km s^{-1} at the base. The lower crust V_p increases from 6.5 (± 0.2) km s^{-1} at the top to 7.0-7.2 (± 0.4) km s^{-1} at the base, over a thickness of ~4.5 (+0.5/-0.2) km. The total crustal thickness is observed to be ~7.0-7.5 (+0.2/-0.6) km.

Additional WA seismic profiles in the study region - Profiles A (Stratford et al. 2015), B (Funnell et al. 2017) and P03 (Contreras-Reyes et al. 2010) - sample the background oceanic crust to distances further from the LRSC. One-dimensional velocity-depth profiles through these models (Fig. 13f,g) show a crustal structure consisting of a thin (few hundred metres) sedimentary cover, a <1 km-thick upper crust with velocity increasing from ~3 km s^{-1} to ~5 km s^{-1}, a 1-2 km-thick mid-crust (V_p = 5.0-6.0 km s^{-1}) thickening towards the LRSC, and a ~5 km-thick lower crust with velocity increasing above 7.0 km s^{-1}. The total crustal thickness lies in the range of 6.0-7.5 km, consistent with the lower bound

of White et al. (1992). The results from Profile C are not inconsistent with these observations, despite it sampling a shorter distance away from the LRSC than the other profiles. However, sampling of Profiles A, B and P03 closer to the seamount edifices shows an improved correspondence with the crustal thickness observations from Profile C (Fig. 13g), indicating that there may be a relatively small component of thickening or downwards flexure of the crust. Evidence to support the loading effect of LRSC volcanoes can be seen in the dip of the middle and lower crustal velocity contours towards the seamount chain (Figs 13a-e).

8.2 LRSC

A striking feature of the *forward model* is the existence of anomalous regions with V_p >6.0 km s^{-1} beneath Osbourn and 27.6°S seamounts (Fig. 14a). The apex of each of these features is located 1.0-1.5 km below the seamount summit, has a diameter of ~10 km, about a third to a half of their basal diameter, and protrudes ~5-6 km above the equivalent velocity contours in the saddles between seamounts and ~2-3 km above the bathymetry of the background Pacific plate. All intersecting *TOTAL* profile models (Figs 14a-d) are consistent with respect to the different modelling methodologies adopted, although the Profile C *forward model* presented here displays generally slower (by ~0.2-0.6 km s^{-1}; Fig. 14e) velocities and a smaller overall crustal thickness (<1.0 km) than that shown by Profile P03 (Contreras-Reyes et al. 2010).

Contreras-Reyes et al. (2010) calculate that ~60% of 27.6°S seamount (by volume) is associated with the intrusive core. However, this result is dependent on the velocity definition for the intrusive-extrusive transition (e.g. Houtz & Ewing 1976; White et al. 1992; Kopp et al. 2004). Assuming radial symmetry, we find similar values of ~50-67% for Osbourn seamount for a range of velocity transitions between 6.0-6.5 km s^{-1}. Calculating the intrusive-extrusive ratio for 27.6°S seamount using the results of this study is challenging as Profile C done not traverse exactly through the centre of the seamount summit and, therefore, the assumption of radial symmetry does not fully hold. However, given our along-LSRC model structures and ratios (where calculable) for Osbourn and 27.6°S seamounts show consistency with the across-LRSC model of Contreras-Reyes et al. (2010), a value of ~60% may be regarded as representative of LRSC seamounts that do have elevated velocity anomaly cores.

Not all seamounts imaged by Profile C display the internal structure described above. Canopus seamount has a less pronounced velocity anomaly core (Fig. 14a). Where sampled by Profile B (Funnell et al. 2017), this seamount and the trench-ward flank of Osbourn seamount sampled by Profile A (Stratford et al. 2015), also lack evidence for a shallow elevated velocity anomaly (Fig. 14c & d). However, each of these profiles also do not cross directly over their associated seamount summit (Fig. 1b) and may, in turn, suggest that these intrusive bodies are laterally discrete.

In the saddles between these three seamounts, the upper and middle crust display thicknesses of ~1.0-1.5 (± 0.2) km and ~3.0-4.0 (± 0.3) km respectively (Fig. 14a). This thickening relative to the background plate is accommodated both as an up to 2 km elevated seabed topography relative to the

background plate and as downward crustal thickening and/or flexure (Fig. 14b), although the Moho depth remains effectively constant, within the model uncertainty, along the LSRC as a whole (Fig. 14a). Much of the thickened upper crust has a velocity of <6.0 km s^{-1}, similar to the seamount flanks. Therefore, we suggest that it dominantly comprises the same material; namely extrusive volcanics and volcaniclastics, and the products of mass wasting and reworking of seamount flank materials. Partially continuous and irregular MCS reflectors are observed in the saddles between seamounts in the restacked MCS section (Figs 12e & f; 330-345 km and 600-625 km d.a.p.), supporting the interpretation that this material is not massive basalt. These shallow reflectors also dip towards the younger end of the seamount chain, and may represent palaeo-flanks and suggest that LRSC seamounts formed by multiple phases of eruption. Distinguishing between intra-seamount saddle and seamount flank material once subducted may, therefore, not be possible based on P-wave velocity alone. This has implications for the ability to image the continuation of the seamount chain if it is oriented directly along Profile C.

Compared to the surrounding oceanic crust imaged in Profiles A, B and P03, the *forward model* shows deepening of the Moho by ~2 km to ~14 km beneath the LRSC (Fig. 14). Within the model resolution, a good fit of observed travel-time picks is achieved with an essentially flat Moho along-strike. The typical LRSC intra-volcanic spacing is 40-80 km, and large volcanoes show an across-track flexural half-width of 40-50 km (Contreras-Reyes et al. 2010). It is, therefore, possible that the along-strike crustal flexure signatures might overlap such that the individual flexural contribution of each edifice cannot be individually resolved in this direction, resulting in this apparent Moho flatness. The only other *TOTAL* profile (P03) to cross the LSRC away from the region of subduction-related plate bend, shows ~2 km deepening of the Moho beneath 27.6°S seamount relative to the adjacent crust (Fig. 14b – Contreras-Reyes et al. 2010), and a Moho depth consistent with our model.

At the LSRC-trench intersection, swath bathymetric data indicates the presence of large-scale normal faults associated with bending of the Pacific plate as it passes over the outer rise (Fig. 2; Bodine & Watts 1979). Where these faults can be traced adjacent to and into Osbourn seamount, they are spaced approximately 5-8 km apart and have vertical offsets of between ~200-800 m. This is significantly less than the up to 2 km throw which is observed on faults to the north and south of the collision zone (Pelletier & Dupont 1990; Crawford et al. 2003; Funnell et al. 2014; 2017), suggesting that the LRSC may act as a moderator to bending and bend-related faulting. A potential effect of this bend-related normal faulting is that a subducting seamount may be vertically disarticulated. If the resulting fragments entering the trench fall below the model horizontal resolution limits of ~12-15 km, which may be possible given the 5-8 km fault spacing, then this may prevent them from being resolved with the seismic reflection and refraction data.

Subduction-related bend faulting may also act as a conduit for the addition of fluid into the down-going crust and mantle, with faults having been shown to cut >20 km down into the mantle at other subduction systems (e.g. Ranero et al. 2003; Ranero & Sallares 2004). Fluid infiltration and associated serpentinisation has the potential to cause velocity reductions of 0.4-0.7 km s^{-1} and ~0.5 km s^{-1} in the

crust and mantle respectively (Ranero et al. 2003; Ivandic et al. 2010; Moscoso & Grevemeyer 2015). Along Profile B, Funnell et al. (2017) show upper- and mid-crust velocities are reduced by ~1 km s^{-1}, and upper mantle velocities by up to 0.5 km s^{-1} in the vicinity of the trench. It is possible that this process may accommodate the 110 kg m^{-3} decrease in the mantle density for the Pacific plate relative to the overriding plate that is required to produce the best-fit gravity model (Fig. 11). This density decrease corresponds to a velocity reduction of ~0.2-0.3 km s^{-1} which lies within the confidence limits of the mantle velocity for this plate (+0.4/-0.2 km s^{-1}). Hence, for the Profile C models the velocity manifestation of local mantle hydration may not be resolvable.

8.3 Indo-Australian plate

Where Profile C crosses the Tonga forearc it displays a slope-basin-slope morphology (Figs 1 & 3). The lower trench slope, between 0-35 km distance perpendicular to trench (d.p.t. – Fig. 8), or ~185-245 km d.a.p., is uplifted, dips toward the trench at ~3-4°, and is covered by little-to-no sediment (Fig. 3b). Further up-slope, between ~35-75 km d.p.t. (~120-180 km d.a.p.), the broadly flatter mid-trench slope is crossed by a number of ~800-900 m high ridges orientated sub-parallel to the trench, which bound small basins. Limited sediment fill in these basins suggests that they are relatively young features, and that the upper trench slope has not yet been significantly eroded, which will lead to the re-equilibration of slope morphology over time.

The forearc upper crust (V_p <5.0 km s^{-1}) has a minimum thickness of ~2.0-2.5 (± 0.2) km between 50-90 km d.p.t. (~100-180 km d.a.p.), increasing to ~4 km at the lower trench slope and towards the arc (Fig. 15b), which is generally consistent with the observations along *TOTAL* Profiles A, B and P03 (Figs 15 a, d & e). In the uplifted lower trench slope region (0-40 km d.p.t.), the uppermost crustal velocity is reduced from ~3.5 km s^{-1} to ~3.2 km s^{-1}, a feature also observed along Profiles A and B (Figs 15d & e). Observations of normal and reverse faults in cored sections from ODP Site 841 on the forearc slope (Ballance et al. 1989; MacLeod 1994) support the interpretation that seamount subduction may be accommodated by permanent deformation of the overriding plate in the form of compression and uplift, followed by subsequent extension and gravitational collapse as the topographic feature is subducted beyond the base of this region (Dominguez et al. 1998).

The forearc middle crust is generally uniform (~2.0 ± 0.3 km) in thickness, and dips towards the trench. The *inverse model* displays a lower velocity (V_p <6.0 km s^{-1}) region at 8-12 km depth between 0-40 km d.p.t. (~180 km d.a.p.), adjacent to an ~3 km shallowing of the 6.0 km s^{-1} contour arcward of 40 km d.p.t. (Fig. 12c). Comparable features exist at similar offsets from the trench axis in Profiles B and P02, and to a lesser extent in Profile A (Figs 15e, a & d respectively). However, these features are not apparent in the *forward model* of Profile C (Fig. 15b), although the lower ray coverage in this part of the model (Fig. 8b) means that it is less well constrained.

The lower crust is up to 8 km thick, with velocity increasing to ~7.0 (± 0.4) km s^{-1} at the Moho. A shallowing of the 6.5 km s^{-1} contour, from ~10.0 km to ~7.5 km b.s.s. between 80-130 km d.p.t. (~30-

120 km d.a.p.), is interpreted as representing the Tonga Ridge, the buried Eocene initial arc. Due to the oblique direction at which Profile C crosses the forearc, the apparent width of this feature is greater than its true width of ~40-50 km as observed on Profiles A and B (Figs 15d & e; Stratford et al. 2015; Funnell et al. 2017). This feature is observed to extend laterally along-trench-strike north to the 18-19°S Fonualei Discontinuity (Fig. 1a; e.g. Crawford et al. 2003; Contreras-Reyes et al. 2010), and south to the 32°S Discontinuity (e.g. Bassett et al. 2016; Funnell et al. 2017), suggesting that it pre-dates, and as such is not a consequence of, seamount subduction.

The *forward model* displays an uppermost mantle velocity beneath the overriding plate of ~7.8 km s^{-1}, which is ~0.2 km s^{-1} slower than beneath the Pacific plate, and which may be a result of hydration by fluid transfer from subducted material (Carlson & Miller 2003; Hyndman & Peacock 2003; Contreras-Reyes et al. 2011). Gravity modelling appears to indicate that the reverse is true, as the *density model* has an Indo-Australian plate mantle density 110 kg m^{-3} higher than that of the Pacific mantle (Fig. 11). However, Table 2 shows that the poor constraint on the mantle velocity of the overriding plate results in the sensitivity limit allowing such variation in density in order to achieve a good fit. The apparently opposing results here are, therefore, not inconsistent and can be accommodated within the modelling resolutions of both the seismic and gravity approaches. It is possible that melt depletion may result in small variations in mantle seismic velocity and density (Schutt and Lesher, 2006), however, these are likely to be below the model confidence limits in this case.

An ~50 mGal positive gravity anomaly misfit in the region of the trench axis and lower forearc slope (Fig. 11a, green line) may indicate that laterally continuous density blocks across each plate do not produce the best fit. Reducing the density of the upper crustal blocks by 200 kg m^{-3} and the middle crustal block by 350 kg m^{-3} between 180 km d.a.p. and the trench axis (Fig. 11c), corresponding to relative velocity decreases of ~0.5 km s^{-1} and ~1.0 km s^{-1} respectively, successfully removes this misfit. These reductions lie outside the *forward model* confidence limits for the corresponding layers (+0.4/-0.3 km s^{-1}). However, the challenges associated with imaging velocity-depth structure within the crust in bathymetrically and structurally complex environments, which manifest as regions of highly variable ray coverage (Fig. 8), may suggest that our velocity model is poorly constrained here, or that our confidence limits may be underestimated. This apparent velocity-density ambiguity for the overriding plate adjacent to the subduction interface is not unique to Profile C and, as it is also a feature of the other *TOTAL* profiles, it may be associated with the development of faulting networks in response to seamount subduction (Dominguez et al. 1998; Wang & Bilek 2011).

9. DISCUSSION

9.1 Seamount formation

Seamounts are built by intrusive and extrusive volcanic processes, the combination of which results in variations in crustal structure. Where seamounts possess intrusive cores, such as those present in Osbourn and 27.6°S seamounts (Fig. 14; Contreras-Reyes et al. 2010), it is proposed that these form

during the relatively early stages of volcanism, as the high hydrostatic pressure of deep-water environments is less favourable to volcanic extrusion (Bonatti & Harrison 1988; Kaneda et al. 2010). Decreasing hydrostatic pressure during seamount growth progressively favours extrusion, and outgassing changes from effusive to explosive in type (Staudigel & Clague 2010). The guyot morphology of Louisville Ridge seamounts (Figs 1-3) shows that they were once emergent and have subsequently subsided and been eroded by wave action. Therefore, they must have passed through the effusive-explosive transition at between ~700-1000 m water depth (e.g. Staudigel & Schminke 1984) at some point.

Increased explosive-extrusive volcanism during later periods of seamount growth may produce up to 70% clastic material (Staudigel & Schminke 1984), including hydro- and hyaloclastites and pillow fragment breccias. This process may be enhanced by a decrease in magma temperature over the eruptive period, and associated increase in the crystal:liquid ratio and viscosity, further promoting fracturing during the cooling process (Bonatti & Harrison 1988). The increasing proportion of explosive-extrusive volcanism over time would result in clastic and/or fractured volcanic products being the dominant component of the seamount flanks and proximal areas. As a result of their fractured and potentially chemically altered nature, these materials will tend to show a lower velocity relative to that of massive intrusive cores of similar composition. It is likely that this type of material comprises the observed >5 km thickness sub-seabed of Canopus seamount, and the up to 2 km upward-thickening of the upper oceanic crustal layer (V_p <6.0 km s^{-1}) observed in the saddles between seamounts (Fig. 8). Progressive accumulation of this material over extended periods throughout the eruptive life span of a seamount, may also explain the discontinuous and irregular sub-basement reflectors at shallow depths below the seabed (<2 s TWTT b.s.b.; Figs 12d-f).

This model for seamount formation predicts that a seamount may comprise a discrete intrusive core surrounded by fragmented material. How the transition between intrusive and fragmented material appears in a velocity-depth model will be governed both by whether the change from dominantly intrusive to extrusive/explosive-extrusive volcanism is distinct, or occurs more gradually, and the capability of the imaging technique to resolve gradational (second-order discontinuities) from stepped (first-order discontinuities) changes in velocity. In the Profile C *forward model*, the upper boundary of the intrusive cores is represented as a first-order velocity discontinuity (Fig. 14e), with a depth sensitivity of +0.3/-0.2 km. The apparent lack of a distinct intrusive core at shallow levels beneath Canopus seamount may simply reflect either a more distributed eruptive source, a more gradational transition between intrusive and eruptive products than either Osbourn and 27.6°S seamounts, or indicate the spatially limited extent of the discrete intrusive body.

9.2 Seamount structural diversity

To understand the observed diversity in seamount structure in relation to location and timing of formation, it has been suggested (e.g. Contreras-Reyes et al. 2010; Richards et al. 2013) that the

response of the lithosphere to point sources of magmatism is an expression of vulnerability to shallow vertical intrusion, that scales proportionally to the age of the lithosphere at the time of volcanism (Δt) and to the square root of plate velocity over the magmatic source (Gass et al. 1978; Pollack et al. 1981). The observation of high velocity cores intruded to shallow depths within LRSC volcanoes indicates that, for this hypothesis to hold, the LRSC should exhibit relatively low Δt values. However, determining Δt at the LSRC is challenging due to the limited temporal constraints that exist for the Osbourn Trough palaeo-spreading centre, which result in a range of Δt values of 10-35 Ma for the lithosphere underlying Osbourn seamount (Billen & Stock 2000; Mortimer et al. 2006; Worthington et al. 2006; Downey et al. 2007).

Using the seamount $^{40}Ar/^{39}Ar$ age of 69.65 ± 0.48 Ma (Koppers et al. 2004; 2011) and crustal age of 89.65 ± 1.52 Ma (Müller et al. 2008), a $\Delta t \approx 20$ Ma may be derived for 27.6°S seamount. Individual eruptions are observed in close proximity at several locations along the LRSC over timescales up to 6 Ma (Koppers et al. 2011), indicating that seamount construction may have occurred over extensive timescales, and should be accounted for when considering geochronology and loading histories. Therefore, 20 Ma may represent an upper bound for Δt for 27.6°S seamount. As this seamount formed after Osbourn, and at a greater distance from the Osbourn Trough, Δt for Canopus and Osbourn seamounts cannot be greater than the value for 27.6°S seamount, but the values may also depend on any variation in the rate of migration of the magmatic locus and Osbourn Trough palaeo-spreading rate during LRSC formation.

In contrast to the LRSC, the Hawaiian ($\Delta t \approx$ 60-80 Ma; Watts & ten Brink 1989) and Marquesas ($\Delta t \approx$ 50 Ma; Caress et al. 1995) Islands appear to be characterised by a lack of elevated velocity at shallow depths sub-seabed. Instead, these locations display up to ~7 km thickening of the lower crust, with P-wave velocities of up to 7.9 km s^{-1}. This velocity corresponds to the lower bound for peridotitic lithologies (7.8-8.3 km s^{-1} – Richards et al. 2013), suggesting a mafic-ultramafic composition, in contrast to the LRSC that only displays velocities compatible with a gabbroic composition (V_p <7.2 km s^{-1}). The identification of mid-crustal reflectors consistent with the depth of normal oceanic crust beneath the Hawaiian and Marquesas Islands may, therefore, represent the pre-hotspot Moho below which the mafic-ultramafic magmatic material has accreted resulting in the observed apparent downward crustal thickening (Caress et al. 1995).

Theoretical batch melting experiments show that melting pressure acts as a primary control on resultant density (e.g. Richards et al. 2013). Beneath older lithosphere, melting and melt equilibration with the surrounding mantle rocks will occur deeper than under younger lithosphere. MgO content increases monotonically with melting pressure, with clinopyroxene and olivine replacing plagioclase in the crystallisation assemblage over a pressure range of 0.7-1.5 GPa (e.g. Farnetani et al. 1996), corresponding to a change in melting depth from ~20 km to ~45 km, and resulting in crystallization densities of 2800-2900 kg m^{-3} and >3000 kg m^{-3} respectively. These densities correspond to P-wave velocities of 5.5-6.5 km s^{-1} and >7.0 km s^{-1} (Carlson & Herrick, 1990), which are consistent with the

contrasting structure of the LRSC-type (Fig. 14a,e; V_p = 6.0 km s^{-1} as shallow as ~1.5 km b.s.b., increasing to ≤7.2 km s^{-1} at the base of the crust; ρ ≈ 2700-2900 kg m^{-3}) and Hawaii-type (V_p <6 km s^{-1} within volcanic edifice, V_p = 7.4-7.9 km s^{-1} below pre-hotspot Moho; Richards et al. 2013) proposed intrusive core versus no intrusive core end members.

Richards et al. (2013) propose that the Moho may act as a density filter, with relatively mafic-ultramafic magmas required to undergo extensive fractionation of dense Fe- and Mg-species to pass. The result of this filtering on different magmatic compositions would be differences in the depth at which the magma eventually crystallizes. However, the level of neutral buoyancy is not the only barrier to surface-directed migration, and additional factors related to the rheology and stress regime of the host crust may significantly affect the resultant crustal structure (Parsons et al. 1992; Watanabe et al. 1999; Menand 2011). This may be particularly significant where non-Wilson-Morgan type (Wilson 1963; Morgan 1971) processes provide the mechanism of magmatism. Hence, the resulting seamount crustal structure may not necessarily reconcile with the predictions of the plate age hypothesis. For example, intrusive cores with velocity ≥6.5 km s^{-1} are observed at the Marcus-Wake Seamount Chain (Kaneda et al. 2010), which has a Δt value of ~60 Ma (Koppers et al. 2000). However, a lack of evidence for age progressive magmatism (Winterer et al. 1993; Koppers et al. 2003) and the orientation of the chain relative to surrounding seafloor palaeo-crack fabric (Smoot 1989), suggest that the structure and evolution of these features may be governed primarily by lithospheric and/or crustal controls rather than deep mantle melting anomalies.

9.3 LRSC subduction

Neither the *forward* (Fig. 8) or *inverse* (Fig. 9) *models* display unequivocal evidence for relatively higher velocity at shallow depth in the down-going plate region, which could be interpreted as indicating the presence of a subducting seamount ahead of Osbourn. The restacked MCS data does, however, display a series of sub-horizontal reflectors between 225-240 km d.a.p. and 8.5-9.5 s TWTT (Fig. 13d), that may be analogous to an 8-9 km-long, arcward-dipping reflector beneath the Tonga lower-trench slope at ~25.5°S along the projection of the LRSC interpreted by Ballance et al. (1989) to represent a subducted seamount summit. Alternatively, however, these reflectors may simply represent the top of the down-going plate boundary when TWTT-converted from the *forward model* (Fig. 13c), which in depth does not contain evidence for a subducting seamount.

To determine if a seamount might be imaged beneath the trench slope along Profile C if it were subducted whole, it is necessary to consider the size of the target with respect to the model resolution limits. A typical LRSC seamount has a summit diameter of 20-30 km, a basal diameter of 40-60 km and a prominence above the seafloor of 3-4 km. Comparison of these dimensions with the whole model and trench region horizontal resolution limits of ~15-20 km and 30 km respectively (Fig. 10), indicates that a seamount of this size, if it were subducted intact along the continuation of Profile C, should be resolvable. However, it is observed that Osbourn seamount is extensively normal faulted (Fig. 2), and

several of the 5-8 km thick, fault-bounded blocks would thus have to remain in sufficient proximity for seamounts of its size to be imaged within the *forward model*, if the subducting seamount has been disarticulated. Consequently, the combined modelling results presented in this paper preclude intact subduction of a seamount ahead of Osbourn, if subduction took place along the trend of Profile C. Alternatively, the LRSC may at this point exhibit a westward bend of up to 35° in the strike of the chain, as proposed by Timm et al. (2013) and supported by the residual bathymetry and gravity anomalies of Bassett & Watts (2015), and offset of the centre of the Louisville seismic gap towards the south. In this case, a seamount subducted intact should be imaged by Profile A, and is not (Stratford et al. 2015). However, neither our or the modelling results of Stratford et al. (2015) preclude the possibility that significant seamount disarticulation and disaggregation has occurred during subduction. It is also possible that the continuation of the LRSC pre-Osbourn does not lie directly along Profile C, or any of the other *TOTAL* seismic profiles. The difficulty in distinguishing between intra-seamount saddle and seamount flank material based on observed P-wave velocity alone prevents unequivocal determination of the presence of a subducting seamount along any one of these WA seismic profiles in the absence of observation of either a velocity structure or a geometric feature which can be unambiguously attributed to a seamount edifice.

9.4 Along-margin effects of LRSC subduction

The oblique directions of both the subduction of the Pacific plate and the strike of the LRSC relative to the margin, result in the point of ridge-trench intersection migrating southward over time. This, in turn, leads to the generation of significant along-trench variation in forearc morphology as a direct consequence of seamount subduction. We can apply the Ballance et al. (1989) model for tectonic erosion resulting from a seamount subduction cycle to the observations of resulting forearc structure here.

Prior to seamount collision, 'background' subduction of a sediment-poor incoming plate is characterised by horst and graben causing partial frontal and basal erosion of the lower trench slope (e.g. von Huene and Ranero 2003). Lower forearc seismic velocities of 3-6 km s^{-1}, observed along the length of the TKT (Fig. 15e; Funnell et al. 2017), also support the erosion of forearc material. This leads to steepening and extensional gravitationally-driven collapse of the forearc into the trench (e.g. Clift and MacLeod, 1999).

As a seamount approaches, subduction of the seamount edifice (and associated crustal swell) initiates enhanced uplift, faulting and erosion of the lower forearc. The present LRSC-TKT intersection is marked by an ~4 km shallowing of the trench (Ballance et al., 1989) and the uplift and merger of the mid- and lower-trench slopes (Stratford et al. 2015). This latter observation is distinct from the slope morphology observed to the north (Contreras-Reyes et al. 2011) and south (Funnell et al. 2014; 2017), suggesting it is a result of support from beneath by the subducting bathymetric feature and, therefore,

only temporary. Forearc uplift may also be associated with bulging of the lower forearc slope towards the trench (Fig. 1b).

North of the syn-collisional zone, frontal and basal erosion of the forearc continue as occurs to the south (Ballance et al. 1989). However, due to the significant weakening of the forearc resulting from seamount subduction, this collapse and re-equilibration of the forearc is accelerated following the removal of the underlying subducted seamount. Seamount-related deformation, therefore, is manifest as a wake-effect whose maximum is not fully observed until after collision. The pre- to post-collisional structural transition occurs over an along-arc distance of ~180 km (Stratford et al. 2015) which, for an intersection migration rate of 120-180 mm yr^{-1} (Lonsdale 1986; Ballance et al. 1989), results in transition timescales of 1.0-1.5 Ma. North of ~22-23°S, the trench slopes return to a more typical and constant along-strike structure, indicating that this represents the northerly limit of the zone affected by LRSC subduction (Stratford et al., 2015).

The observations of the along-margin structural variability and evolution show that seamount-related deformation is superimposed on both background tectonic processes and pre-existing crustal structures (e.g. the buried Eocene Tonga Ridge; e.g. Crawford et al. 2003; Funnell et al. 2017). Furthermore, the along-margin observations of trench slope morphology and uplift history discussed here, present-day seismicity (Scholz & Small 1997), and potential field data (Bassett and Watts, 2015), do not negate the possibility that the point of present LRSC-TKT collision is also co-incident with a westward bend in the chain. It is unclear how fault-related disarticulation of seamounts may affect subduction zone seismicity, as structural models of seamount subduction (e.g. Cloos & Shreve 1996; Dominguez et al. 1998; Wang & Bilek 2011) do not consider the effect of disaggregated plate topography in collision with the base of the overriding plate. The presence of the Louisville seismic gap clearly indicates that modification to the background stress pattern prevails at this location. However, given that the width of the seismic gap of ~200 km is approximately equivalent to the width of the across-chain crustal 'swell', it is probable that this is the principal factor affecting seismic processes. Disarticulation of the seamounts does not, therefore, conflict with the observations of reduced seismicity, as it is not necessarily the presence of individual volcanic edifices which results in this pattern.

10. CONCLUSIONS

New velocity- and density-depth models have been presented for a ~750 km-long profile that traverses both the Louisville Ridge Seamount Chain and the Tonga forearc. The robustly tested combined model has been synthesised with other across-LRSC profiles to highlight the three-dimensional crustal structures of Osbourn, Canopus and 27.6°S seamounts. We use our results to consider the likely mode of origin of these seamounts and what their fate might be once they are subducted at the Tonga-Kermadec trench. We conclude that:

1. Most, but not all, of the seamounts of the LRSC display evidence for intrusive magmatic bodies with elevated seismic velocity cores (V_p ≥6.0 km s^{-1}). These cores protrude above the level of the background seafloor to a depth of ~1.0-1.5 km beneath seamount summits, where they have a diameter of about a third to a half of their basal diameter. By volume, these cores represent ~50-67% of the seamount. That these cores are only observed when crossing directly over a seamount summit suggests that they are discrete in their lateral extent given the resolution of the modelling approach adopted.
2. A model of seamount formation that considers variation in the proportion of intrusive-to-extrusive volcanism and the explosive nature of extrusive processes, explains the observation of discrete intrusive cores within the seamounts, and suggests that seamount flanks and intra-seamount saddles comprise volcaniclastic and/or mass-wasted material, consistent with their P-wave seismic velocity.
3. The presence of shallow intrusive bodies and corresponding young plate ages at the time of eruption suggest that plate thermal and mechanical characteristics at the time of volcanism govern the resulting seamount structure, with variability in the depth of melting and fractionation controlling magma composition and buoyancy contrasts between the intruding magma and the host oceanic lithosphere.
4. A typical LRSC seamount has a summit diameter of 20-30 km, a basal diameter of 40-60 km and a prominence above the seafloor of 3-4 km. Modelling resolution suggests that if a seamount of this size were subducted intact in the direction of the continuation of Profile C across the forearc, it should be resolvable. We find no evidence for an intact seamount ahead of Osbourn, and so either disarticulation below the resolution limits has occurred or the current position of the Tonga-Kermadec trench-LRSC intersection correlates with a bend in the strike of the chain, although the velocity-depth model of Profile A does not support intact subduction along a continuation of the chain along that azimuth.
5. Seamount subduction has a direct and significant additional erosive impact on the overriding plate morphology and structure, and plate boundary seismicity, which is superimposed over the 'background' processes of tectonic erosion. However, it does not appear entirely necessary that seamount edifices remain significantly intact during the subduction process for such erosion to occur.

ACKNOWLEDGEMENTS

This research, funded by the Natural Environmental Research Council (NERC) via research grant NE/F004273/1 (Peirce & Watts 2011) together with a quota studentship to AHR, formed part of the *TOTAL* project whose Lead Investigators were Prof. Tony Watts (Oxford), CP and Prof. Ingo Grevemeyer (IFM-Geomar). We are grateful to the three anonymous reviewers for their thoughtful and helpful comments on this paper. We would like to thank all those involved in the planning and acquisition of data during research cruise SO215, including the officers, engineers and crew of the R/V

Sonne, the scientific party, and all seagoing technicians. In addition to technical support at sea, the NERC Ocean-Bottom Instrumentation Facility (Minshull et al. 2005) and IFM-Geomar provided the OBSs, and the NERC National Marine Facility the MCS acquisition system and gravimeter used during SO215. The MCS data were processed using Claritas™ and Seismic Unix. All figures were prepared using the Generic Mapping Tools (Wessel & Smith 1998). Data from cruise SO215 are archived at the NERC British Oceanographic Data Centre (bodc.ac.uk), and the final accepted manuscript version of this paper is available through Durham Research Online (dro.dur.ac.uk).

REFERENCES

Ballance, P.F., Scholl, D.W., Vallier, T.L., Stevenson, A.J., Ryan, H., & Herzer, R.H., 1989. Subduction of a Late Cretaceous Seamount of the Louisville Ridge at the Tonga Trench: A Model of Normal and Accelerated Tectonic Erosion, *Tectonics*, *8*(5), 953–962.

Ballmer, M.D., van Hunen, J., Ito, G., Tackley, P.J., & Bianco, T.A., 2007. Non-hotspot volcano chains originating from small-scale sublithospheric convection, *Geophys. Res. Lett.*, 34, 1–5.

Bassett, D., & Watts, A.B., 2015. Gravity anomalies, crustal structure, and seismicity at subduction zones: 1. Seafloor roughness and subducting relief, *Geochem., Geophys. Geosyst.*, 16, 1508–1540.

Bassett, D., Kopp, H., Sutherland, R., Henrys, S., Watts, A.B., Timm, C., Scherwath, M., Grevemeyer, I., & de Ronde, C.E.J., 2016. Crustal structure of the Kermadec arc from MANGO seismic refraction profiles, *J. Geophys. Res. Solid Earth*, 121, 1–33.

Beier, C., Vanderkluysen, L., Regelous, M., Mahoney, J.J., & Garbe-Schönberg, D., 2011. Lithospheric control on geochemical composition along the Louisville Seamount Chain, *Geochem., Geophys. Geosyst.*, 12(9), 1-19

Bevis, M., Taylor, F.W., Schutz, B.E., Recy, J., Isacks, B.L., Helu, S., Singh, R., Kendrick, E., Stowell, J., Calmant, S., 1995. Geodetic observations of very rapid convergence and back-arc extension at the Tonga arc, *Nature*, 374, 249–251.

Billen, M.I., & Stock, J., 2000. Morphology and origin of the Osbourn Trough, *J. Geophys. Res.*, 105(B6), 13481-13489.

Bodine, J.H., & Watts, A.B., 1979. On lithospheric flexure seaward of the Bonin and Mariana trenches, *Earth Planet. Sci. Lett.*, 43(1), 132–148.

Bonatti, E., & Harrison, C.G.A., 1988. Eruption Styles of Basalt in Oceanic Spreading Ridges and Seamounts: Effect of Magma Temperature and Viscosity, *J. Geophys. Res.*, 93(B4), 2967–2980.

Bonnardot, M.-A., Régnier, M., Ruellan, E., Christova, C., and Tric, E., 2007. Seismicity and state of stress within the overriding plate of the Tonga-Kermadec subduction zone, *Tectonics*, *26*, 1–15,

Cande, S.C., & Kent, D.V., 1992. A New Geomagnetic Polarity Time Scale for the Late Cretaceous and Cenozoic, *J. Geophys. Res.*, 97(B10), 13917–13951.

Caress, D.W., McNutt, M.K., Detrick, R.S., & Mutter, J.C., 1995. Seismic imaging of hotspot-related crust underplating beneath the Marquesas Islands, *Nature*, 373, 600–603.

Carlson, R.L., & Herrick, C.N., 1990. Densities and porosities in the oceanic crust and their variations with depth and age, *J. Geophys. Res.*, 95(B6), 9153-9170.

Carlson, R.L., & Miller, D.J., 2003. Mantle wedge water contents estimated from seismic velocities in partially serpentinized peridotites, *Geophys. Res. Lett.*, 30(5), 1-4.

Clift, P.D., MacLeod, C.J., Tappin, D.R., Wright, D.J., & Bloomer, S.H., 1998. Tectonic controls on sedimentation and diagenesis in the Tonga Trench and forearc, southwest Pacific, *Geol. Soc. Am. Bull.*, 110(4), 483–496.

Clift, P.D., & MacLeod, C.J., 1999. Slow rates of subduction erosion estimated from subsidence and tilting of the Tonga forearc, *Geology*, 27(5), 411-414.

Cloos, M., 1992. Thrust-type subduction-zone earthquakes and seamount asperities: A physical model for seismic rupture, *Geology*, 20, 601–604.

Cloos, M., & Shreve, R.L., 1996. Shear-zone thickness and the seismicity of Chilean- and Marianas-type subduction zones, *Geology*, 24(2), 107–110.

Contreras-Reyes, E., Grevemeyer, I., Watts, A.B., Planert, L., Flueh, E.R., & Peirce, C., 2010. Crustal intrusion beneath the Louisville hotspot track, *Earth Planet. Sci. Lett.*, 289, 323–333.

Contreras-Reyes, E., Grevemeyer, I., Watts, A.B., Flueh, E.R., & Peirce, C., Moeller, S., & Papenberg, C., 2011. Deep seismic structure of the Tonga subduction zone: Implications for mantle hydration, tectonic erosion, and arc magmatism, *J. Geophys. Res.*, 116, 1-18.

Crawford, W.C., Hildebrand, J.A., Dorman, L.M., Webb, S.C., & Wiens D.A., 2003. Tonga Ridge and Lau Basin crustal structure from seismic refraction data, *J. Geophys. Res.*, 108(B4), 2195.

DeMets, C., Gordon, R.G. & Argus, D.F., 2010. Geologically current plate motions, *Geophys. J. Int.*, 181, 1–80.

Dix, C.H., 1955. Seismic velocities from surface measurements, *Geophysics*, *20*(1), 68–86.

Dominguez, S., Lallemand, S.E., Malavieille, J., & von Huene R., 1998. Upper plate deformation associated with seamount subduction, *Tectonophysics*, 293, 207–224.

Downey, N.J., Stock, J.M., Clayton, R.W., & Cande, S.C., 2007. History of the Cretaceous Osbourn spreading center, *J. Geophys. Res.*, 112, 1–18.

England, P., Engdahl, R., Thatcher, W., 2004. Systematic variation in the depths of slabs beneath arc volcanoes, *Geophys. J Int*., 156 (2): 377-408.

Farnetani, C.G., Richards, M.A., & Ghiorso, M.S., 1996. Petrological models of magma evolution and deep crustal structure beneath hotspots and flood basalt provinces, *Earth Planet. Sci. Lett.*, 143, 81–94.

Funnell, M.J., Peirce, C., Stratford, W.R., Paulatto, M., Watts, A.B., & Grevemeyer, I., 2014. Structure and deformation of the Kermadec forearc in response to subduction of the Pacific oceanic plate, *Geophys. J. Int.*, 199, 1286–1302.

Funnell, M. J., C. Peirce, and A. H. Robinson (2017), Structural variability of the Tonga-Kermadec forearc characterized using robustly constrained geophysical data, Geophys. J. Int., 210, 1681–1702.

Gass, I.G., Chapman, D.S., Pollack, H.N., Thorpe, R.S., & C. Froidevaux, C., 1978. Geological and Geophysical Parameters of Mid-Plate Volcanism [and Discussion], *Philos. Trans. R. Soc. A*, 288, 581–597.

Grevemeyer, I., and Flueh, E. R., 2008. FS Sonne Cruise Report SO195: TOTAL TOnga Thrust earthquake Asperity at Louisville Ridge, Suva/Fiji - Suva/Fiji 07.01. - 16.02.2008

Habermann, R.E., McCann, W.R., and Perin, B., 1986. Spatial seismicity variations along convergent plate boundaries, *Geophys. J. R. Astr. Soc.*, *85*, 43–68.

Hayes, G.P., Wald, D.J., & Johnson, R.L., 2012. Slab1.0: A three-dimensional model of global

Houtz, R., & Ewing, J., 1976. Upper crustal structure as a function of plate age, *J. Geophys. Res.*, 81(14), 2490–2498.

Hyndman, R.D., & Peacock, S.M., 2003. Serpentinization of the forearc mantle, *Earth Planet. Sci. Lett.*, 212, 417–432.

Ivandic, M., Grevemeyer, I., Bialas, J., and Petersen, C.J., 2010. Serpentinization in the trench-outer rise region offshore of Nicaragua: Constraints from seismic refraction and wide-angle data, *Geophys. J. Int.*, 180(3), 1253–1264.

Kaneda, K., Kodaira, S., Nishizawa, A., Morishita, T., & Takahashi, N., 2010. Structural evolution of preexisting oceanic crust through intraplate igneous activities in the Marcus-Wake seamount chain, *Geochem., Geophys. Geosyst.*, 11(10), 1-29.

Kopp, H., 2013. Invited review paper: The control of subduction zone structural complexity and geometry on margin segmentation and seismicity, *Tectonophysics*, 589, 1–16.

Kopp, H., Flueh, E.R., Papenberg, C., & Klaeschen, D., 2004. Seismic investigations of the O'Higgins Seamount Group and Juan Fernández Ridge: Aseismic ridge emplacement and lithosphere hydration, *Tectonics*, 23, 1-21.

Koppers, A.A.P., Staudigel, H., & Wijbrans, J.R., 2000. Dating crystalline groundmass separates of altered Cretaceous seamount basalts by the 40Ar/39Ar incremental heating technique, *Chem. Geol.*, 166, 139–158.

Koppers, A.A.P., Staudigel, H., Pringle, M.S., & Wijbrans, J.R., 2003. Short-lived and discontinuous intraplate volcanism in the South Pacific: Hot spots or extensional volcanism?, *Geochem, Geophys. Geosyst.*, 4(10), 1-49.

Koppers, A.A.P., Duncan, R.A., & Steinberger, B., 2004. Implications of a nonlinear $^{40}Ar/^{39}Ar$ age progression along the Louisville seamount trail for models of fixed and moving hot spots, *Geochem. Geophys. Geosyst.*, 5(6), 1-22.

Koppers, A.A.P., Gowen, M.D., Colwell, L.E., Gee, J.S., Lonsdale, P.F., Mahoney, J.J., & Duncan, R.A., 2011. New $^{40}Ar/^{39}Ar$ age progression for the Louisville hot spot trail and implications for inter-hot spot motion, *Geochem. Geophys. Geosyst.*, 12(12), 1-25.

Kuo, B.-Y., Forsyth, D.W., 1988. Gravity anomalies of the ridge-transform system in the South Atlantic between 31 and 34.5°S: Upwelling centers and variations in crustal thickness, *Mar. Geophys. Res.*, 10, 205–232.

Lallemand, E., Malavieille, J., and Calassou, S., 1992. Effects of Oceanic Ridge Subduction on Accretionary Wedges: Experimental Modeling and Marine Obervations, *Tectonics*, *11*(6), 1301–1313.

Lonsdale, P.F., 1986. A multibeam reconnaissance of the Tonga trench axis and its intersection with the Louisville guyot chain, *Mar. Geophys*. Res., 8, 295–327.

MacLeod, C.J., 1994. Structure of the outer Tonga forearc at site 841, in *Proceedings of the Ocean Drilling Program, Scientific Results, College Station, TX (Ocean Drilling Program)*, Vol. 135, pp. 313–329.

McGeary, S., Nur, A., and Ben-Avraham, Z., 1985. Spatial gaps in arc volcanism: The effect of collision or subduction of oceanic plateaus, *Tectonophysics*, 119, 195–221.

Meffre, S., Falloon, T.J., Crawford, T.J., Duncan, R.A., Bloomer, S.H., & Wright, D.J., 2012. Basalts erupted along the Tongan fore arc during subduction initiation: Evidence from geochronology of dredged rocks from the Tonga fore arc and trench, *Geochem. Geophys. Geosyst.*, 13(12), 1–17.

Menand, T., 2011. Physical controls and depth of emplacement of igneous bodies: A review, *Tectonophysics*, 500, 11–19.

Minshull, T.A., Sinha, M.C. & Peirce, C., 2005. Multi-disciplinary, sub- seabed geophysical imaging—a new pool of 28 seafloor instruments in use by the United Kingdom Ocean Bottom Instrument Consortium, *Sea Technol.*, 46, 27–31.

Morgan, W.J., 1971. Convection Plumes in the Lower Mantle, *Nature*, 230, 42–43.

Mortimer, N., Hoernle, K., Hauff, F., Palin, J.M., Dunlap, W.J., Werner, R., & Faure, K., 2006. New constraints on the age and evolution of the Wishbone Ridge, southwest Pacific Cretaceous microplates, & Zealandia-West Antarctica breakup, *Geology*, 34(3), 185–188.

Moscoso, E., & Grevemeyer, I., 2015. Bending-related faulting of the incoming oceanic plate and its effect on lithospheric hydration and seismicity: A passive and active seismological study offshore Maule, Chile, *J. Geodyn.*, 90, 58–70.

Müller, R.D., Sdrolias, M., Gaina, C., & Roest, W.R., 2008 Age, spreading rates, & spreading asymmetry of the world's ocean crust, *Geochem. Geophys. Geosyst.*, 9(4), 1–19.

Nafe, J.E., & Drake, C.L., 1957. Variation With Depth in Shallow and Deep Water Marine Sediments of Porosity, Density and the Velocities of Compresional and Shear Waves, *Geophysics*, XXII(3), 523–552.

Nichols, A.R.L., Beier, C., Brandl, P.A., Buchs, D.M., & Krumm, S.H., 2014. Geochemisty of volcanic glasses from the Louisville Seamount Trail (IODP Expedition 330): Implications for eruption environments and mantle melting, *Geochem. Geophys. Geosyst.*, 15, 1718–1738.

Parsons, T., Sleep, N.H., & Thompson, G.A., 1992. Host rock rheology controls on the emplacement of tabular intrusions: Implications for underplating of extending crust, *Tectonics*, 11(6), 1348–1356.

Peirce, C., and Watts, A.B., 2011. R/V Sonne SO215 Cruise Report. The Louisville Ridge - Tonga Trench collision: Implications for subduction zone dynamics, 1-76.

Pelletier, B., & Dupont, J., 1990. Effets de la subduction de la ride de Louisville sur l'arc de Tonga-Kermadec, *Oceanol. Acta*, 10, 57–76.

Pollack, H.N., Gass, I.G., Thorpe, R.S., & Chapman, D.S., 1981. On the vulnerability of lithospheric plates to mid-plate volcanism: Reply to comments by P. R. Vogt, *J. Geophys. Res.*, 86(B2), 961–966.

Ranero, C.R., & Sallarès, V., 2004. Geophysical evidence for hydration of the crust and mantle of the Nazca plate during bending at the north Chile trench, *Geology*, 32(7), 549–552.

Ranero, C.R., Morgan, J.P., McIntosh, K., & Reichert, C., 2003. Bending-related faulting and mantle serpentinization at the Middle America trench., *Nature*, 425(6956), 367–373.

Richards, M., Contreras-Reyes, E., Lithgow-Bertelloni, C., Ghiorso, M., & Stixrude, L. 2013. Petrological interpretation of deep crustal intrusive bodies beneath oceanic hotspot provinces, *Geochem. Geophys. Geosyst.*, 14(3), 604–619.

Rosenbaum, G., & Mo, W., 2011. Tectonic and magmatic responses to the subduction of high bathymetric relief, *Gondwana Res.*, 19(3), 571–582.

Ruellan, E., Delteil, J., Wright, I., & Matsumoto, T., 2003. From rifting to active spreading in the Lau Basin - Havre Trough backarc system (SW Pacific): Locking/unlocking induced by seamount chain subduction, *Geochem. Geophys. Geosyst.*, 4(5), 1-21.

Sandwell, D.T., Winterer, E.L., Mammerickx, J., Duncan, R.A., Lynch, M.A., Levitt, D.A., & Johnson, C.L., 1995. Evidence for diffuse extension of the Pacific plate from Pukapuka ridges and cross-grain gravity lineations, *J. Geophys. Res.*, 100(B8), 15087–15099.

Scholz, C.H., & Small, C., 1997. The effect of seamount subduction on seismic coupling, *Geology*, 25(6), 487-490

Schutt, D.L., & Lesher, C.E., 2006. Effects of melt depletion on the density and seismic velocity of garnet and spinel lherzolite, *J. Geophys. Res.*, 111, B05401.

Smoot, N.C., 1989. The Marcus-Wake seamounts and guyots at paleo-fracture indicators and their relation to the Dutton Ridge, *Mar. Geol.*, 88, 117–131.

Staudigel, H., & Clague, D.A., 2010. The Geological History of Deep-Sea Volcanoes: Biosphere, Hydrosphere and Lithosphere Interactions, *Oceanography*, 23(1), 58-71.

Staudigel, H., & Schminke, H.-U., 1984. The Pliocene Seamount Series of La Palma / Canary Islands, *J. Geophys. Res.*, 89(B13), 11195–11215.

Stratford, W., Peirce, C., Paulatto, M., Funnell, M., Watts, A.B., Grevemeyer, I, & Bassett, D., 2015. Seismic velocity structure and deformation due to the collision of the Louisville Ridge with the Tonga-Kermadec Trench, *Geophys. J. Int.*, 200, 1503–1522.

Talwani, M., Worzel, J.L., & Landisman M., 1959. Rapid Gravity Computations for Two-Dimensional Bodies with Application to the Mendocino Submarine Fracture Zone, *J. Geophys. Res.*, 64(1), 49–59.

Timm, C., Bassett, D., Graham, I.J., Leybourne, M.I., de Ronde, C.E.J., Woodhead, J., Layton-Matthews, D., & Watts, A.B., 2013. Louisville seamount subduction and its implication on mantle flow beneath the central Tonga-Kermadec arc., *Nat. Commun.*, 4:1720, 1-8.

von Huene, R. & Scholl, D.W., 1991. Observations at convergent margins concerning sediment subduction, subduction erosion, and the growth of continental crust, *Rev. Geophys.*, 29, 279–316.

von Huene, R., & Ranero, C.R., 2003. Subduction erosion and basal friction along the sediment-starved convergent margin off Antofagasta, Chile, *J. Geophys. Res.,* 108(B2), 1-17.

Wang, K., & Bilek, S.L., 2011. Do subducting seamounts generate or stop large earthquakes?, *Geology*, 39(9), 819–822.

Watanabe, T., Koyaguchi, T., & Seno, T., 1999. Tectonic stress controls on ascent and emplacement of magmas, *J. Volcanol. Geotherm. Res.*, 91, 65–78.

Watts, A. B., & ten Brink, U.S., 1989. Crustal structure, flexure, and subsidence history of the Hawaiian Islands, *J. Geophys. Res.*, 94(B8), 10473–10500.

Watts, A.B., ten Brink, U.S., Buhl, P., & Brocher, T.M., 1985. A multichannel seismic study of lithospheric flexure across the Hawaiian-Emperor seamount chain, *Nature*, 315(6015), 105–111.

Wessel, P., & Smith, W., 1998. New, improved version of Generic Mapping Tools released, *Eos.*, 79, 579.

White, R.S., McKenzie, D., & O'Nions, K., 1992. Oceanic Crustal Thickness from Seismic Measurements and Rare Earth Element Inversions, *J. Geophys. Res.*, 97(B13), 19683–19715.

Wilson, J.T., 1963. A Possible Origin of the Hawaiian Islands, *Can. J. Phys.*, 41, 863–870.

Winterer, E.L., Natland, J.H., van Waasbergen, R.J., & Duncan, R.A, 1993. Cretaceous Guyots in the Northwest Pacific: an Overview of Their Geology and Geophysics, *in The Mesozoic Pacific Geology, Tectonics and Volcanism, Geophys. Monogr. 77*, 307-334.

Worthington, T.J., Hekinian, R., Stoffers, P., Kuhn, T., & Hauff, F., 2006. Osbourn Trough: Structure, geochemistry and implications of a mid-Cretaceous paleospreading ridge in the South Pacific, *Earth Planet. Sci. Lett.*, 245, 685–701.

Wright, D.J., Bloomer, S.H., MacLeod, C.J., Taylor, B. & Goodlife, A.M., 2000. Bathymetry of the Tonga Trench and Forearc: a map series, *Mar. Geophys. Res.*, 21, 489–511.

Zelt, C.A., 1998. Lateral velocity resolution from three-dimensional seismic refraction data, *Geophys. J. Int.*, 135, 1101–1112.

Zelt, C.A., 1999. Modelling strategies and model assessment for wide-angle seismic traveltime data, *Geophys. J. Int.*, 139, 183–204.

Zelt, C.A., & Smith, R.B., 1992. Seismic traveltime inversion for 2-D crustal velocity structure, *Geophys. J. Int.*, 108, 16–34.

Zelt, C.A., & Barton, P.J., 1998. Three-dimensional seismic refraction tomography: a comparison of two methods applied to data from the Faeroe Basin, *J. Geophys. Res.,* 103(B4), 7197–7210.

TABLES

Table 1: *Forward model* ray tracing statistics and fit parameters. Note: 1- OBSs C38-C43 have P_g travel-time pick error = 100 ms and P_mP and P_n error = 120 ms; 2 - OBSs located close to the bend in Profile C have an additional travel-time pick error applied to P_g and P_n where picks have been selected as meeting the criteria outlined in Section 4.1.2. Subscripts l and r for P_s and P_g indicate where these phase assignments have been split for the purposes of modelling.

Phase	**Error (ms)**	**Number**	**T_{rms} (ms)**	**χ^2**
P_w	30	14621	32	1.11
$P_{s,l}$	40	270	80	4.03
$P_{s,r}$	40	336	43	1.18
$P_{g,l}$	70[1,2]	12694	109	2.37
$P_{g,r}$	70[1,2]	12369	117	2.63
P_mP	100[1,2]	11619	132	1.72
P_n	100[1,2]	23448	168	2.76
Crustal total (excl. P_w)		**60736**	**140**	**2.45**

Table 2: Best-fit WA *forward model* sensitivity testing results. Values given are the positive and negative perturbations for each test type required to cause the model to diverge from the unperturbed fit values at the top of each table section, beyond threshold fit values of χ^2 >3.0 and χ^2 >3.6 for the overriding and subducting plates respectively. Notes on additional symbols: † - tests cannot be performed as they represent the seabed, which cannot be varied. * - test types are identical in nature due to the presence of a second-order velocity discontinuity in the model (see main text). # - due to the second-order discontinuity at the boundary of this layer, this is not a truly independent test of a change to a single layer (see main text). lv – indicates that this test suffers from layer-crossing violations and, therefore, either fails or reaches a limit beyond which the value cannot be varied further along the whole model. fc – a number of tests in this set fail to run before reaching the quoted sensitivity values, therefore it is likely that the true limits are smaller than those listed.

Plate		**Number of rays**	**T_{rms} (ms)**	**χ^2**	**χ^2 threshold**
Both	P_s only	606	43	1.17	1.9
	All rays	60736	140	2.45	3.5
Overriding / Indo-Australian		20370	119	1.99	3.0
Subducting / Pacific		43940	147	2.59	3.6

Layer		**Layer number**	**Depth (km)**	**Layer top velocity (km s^{-1})**	**Layer bottom velocity (km s^{-1})**	**Layer bulk velocity (km s^{-1})**
Sediment, P_s only		4	not testable†	+0.1/-0.1	+0.3/-0.1	+<0.1/-<0.1
Sediment, all rays			not testable†	+0.4/-0.3^{fc}	+0.3^{fc}/-0.4^{fc}	+0.2/-0.1
Indo-Australian	Crust	5	+<0.2/-<0.1^{lv}	+0.4/-0.2	+0.1/-0.3	+0.1/-0.4^{fc}
		6	+0.3/-0.4	+0.4/-0.3	+0.2/-0.2*	+0.2/-0.1$^{\#}$
		7	+0.4/-0.5	+0.2/-0.2*	+0.4/-0.4	+0.1/-0.1$^{\#}$
	Mantle	8	+0.9/-1.4	insensitive/-0.4	insensitive	+0.4/-0.3
Pacific	Crust	9	+0.075/fail^{lv}	+0.5^{fc}/-0.4	+0.2^{fc}/-0.5	+0.6/-0.3
		10	+0.3/-0.2^{lv}	+0.5/-0.3	+0.4/-0.1*	+0.3/-0.3$^{\#}$
		11	+0.5^{fc}/-0.2	+0.4/-0.1*	+>0.5/-0.3	+0.3/-0.1$^{\#}$
	Mantle	12	+0.2/-0.6	+0.4/-0.2	insensitive	+0.4/-0.2

FIGURES

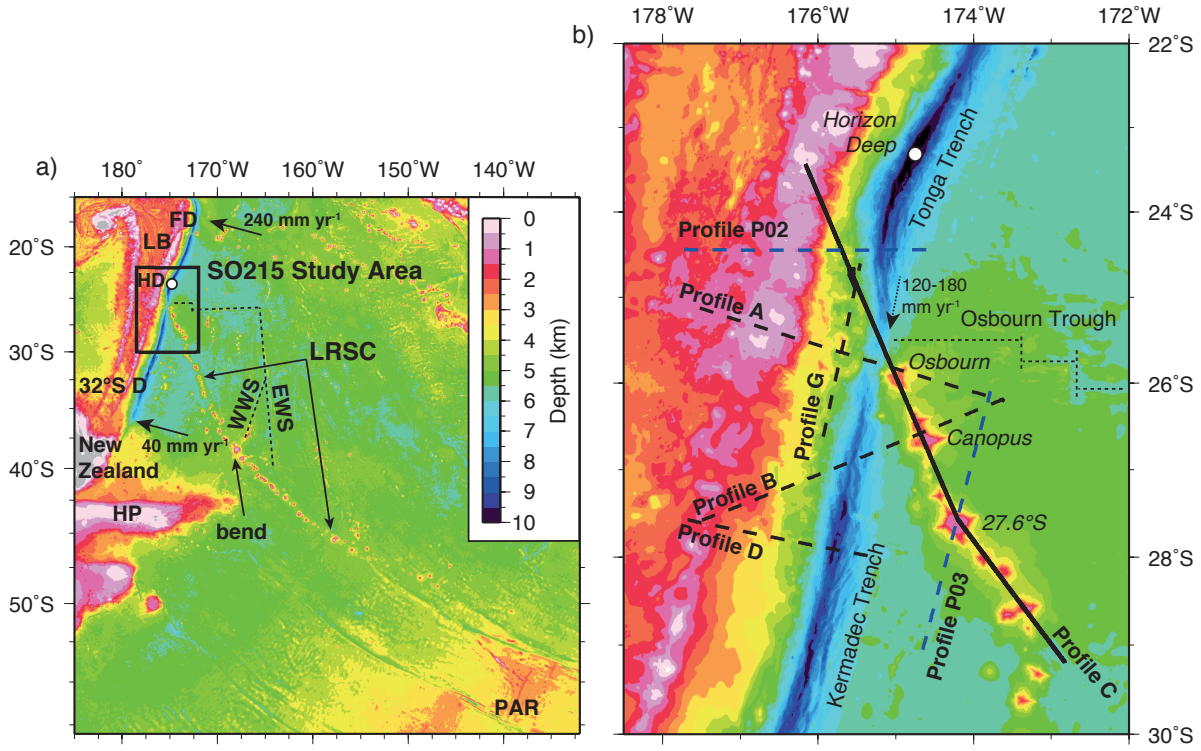

Figure 1: Regional context. a) Regional bathymetry of the SW Pacific (IOC et al., 2003) showing the full extent of the LRSC. Features labelled are: EWS – East Wishbone Scarp, FD – Fonualei Discontinuity, HD – Horizon Deep, HP – Hikurangi Plateau, LB – Lau Basin, LRSC – Louisville Ridge Seamount Chain, PAR – Pacific-Antarctic Ridge, WWS – West Wishbone Scarp, 32°S D – 32°S Discontinuity. Subduction directions and velocities are shown with arrows. Black box shows the location of the SO215 study area, with detail in b). b) Combined satellite-swath bathymetry map of the SO215 study area. Solid black line shows the location of the WA-MCS Profile C. Black dashed lines are additional profiles from the SO215 experiment. Blue dashed lines are profiles from SO195. WA profiles (bold), named seamounts (italics), and trench segments/regional features are labelled. Dotted black line indicates location of the Osbourn Trough palaeo-spreading centre. Arrow indicates the direction and rate of intersection point migration. White circle indicated location of Horizon Deep, the maximum depth of the Tonga Trench.

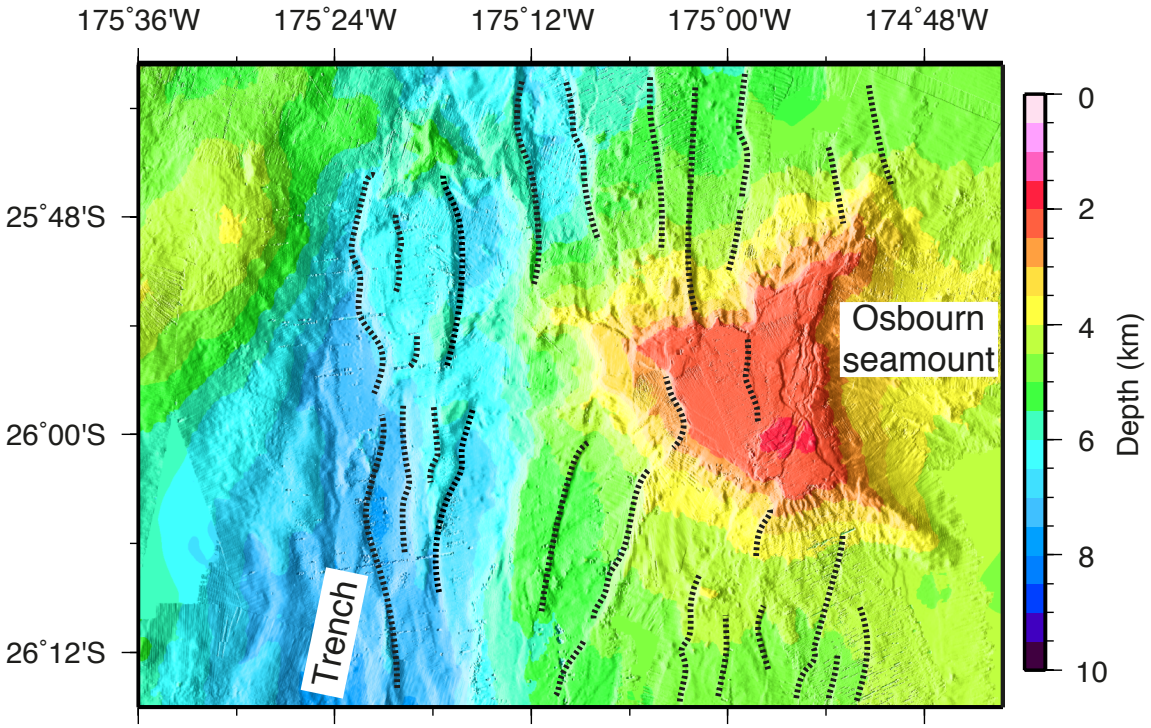

Figure 2: Bathymetric map of Osbourn seamount and adjacent trench area. Dotted lines show locations of bending-associated normal faulting identified on the down-going plate.

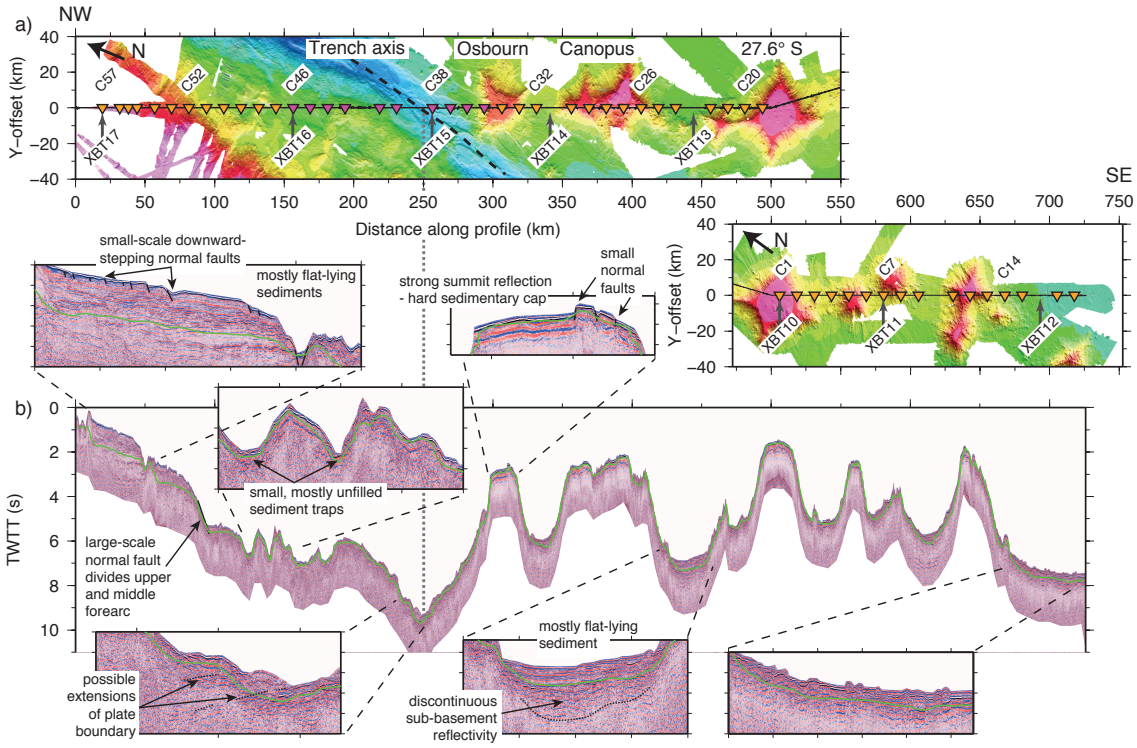

Figure 3: MCS images of key tectonic features. a) Bathymetry of the northern section of Profile C (upper panel – forearc to 27.6°S seamount), and southern section (lower panel – 27.6°S seamount southwards), projected into kilometre-offset modelling space and aligned at the bend in profile. In both cases, Profile C is oriented along y = 0, with shot locations marked by the solid black line. Relocated-onto-profile OBS positions are plotted as inverted triangles coloured orange for OBIF LC-type and purple for IFM-Geomar KUM-type instruments respectively. XBT sampling locations are indicated by grey arrows. Selected OBSs and all XBTs are labelled. b) Profile C MCS data processed as described in the text using a velocity analysis-derived stacking velocity model, post-stack Kirchhoff time-migration at 1.5 km s^{-1}, and displayed with a cosmetic seabed mute and automatic gain control (AGC) with a 2000 ms time gate. Green line indicates the location of the picked sediment-basement interface used to parameterise the initial forward model (see text).

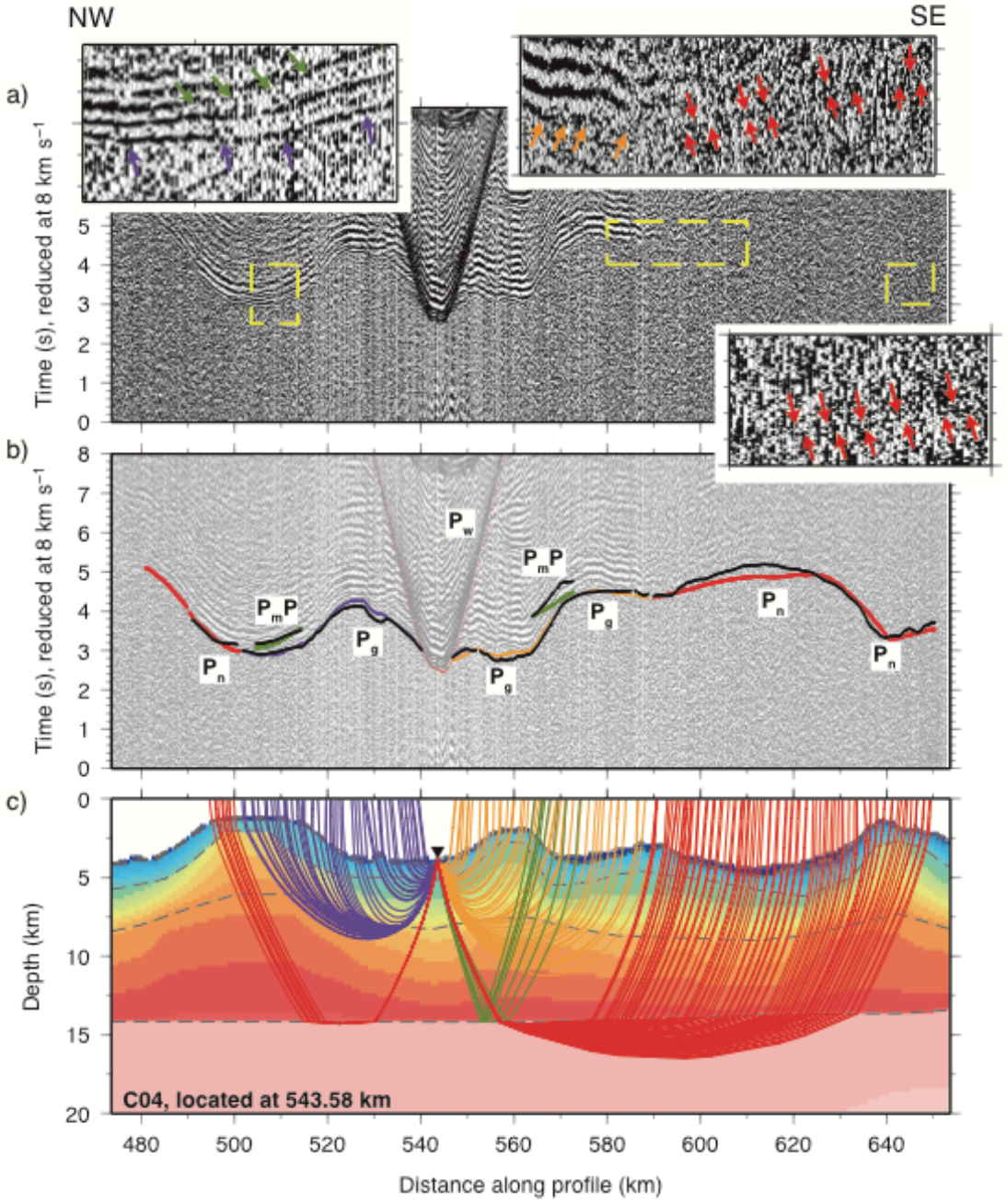

Figure 4: WA seismic data from OBS C04, located at 543.58 km d.a.p. on the southern section of Profile C, to the southeast of 27.6°S seamount at 543.58 km d.a.p. (cf. Fig. 3a). a) OBS record section, displayed using a minimum-phase Butterworth band-pass filter (2-3-20-30 Hz) and reduced at 8.0 km s^{-1}. Insets: Enlarged sections of far-offset arrivals for regions indicated by dashed yellow boxes. Arrows show the location of the picked arrival branch, with colours corresponding to the phase type listed in b). b) OBS record section plotted as in a), with picked phases annotated as coloured bars (dark blue and light blue – P_s; purple and orange – P_g; green – P_mP; red – P_n). Coloured bar length corresponds to pick uncertainty. Black lines show the modelled arrivals. c) Calculated rays traced through the best-fit *forward model*, where the ray colours match picked phase sets in b). Inverted triangle indicates the re-located OBS position in the model.

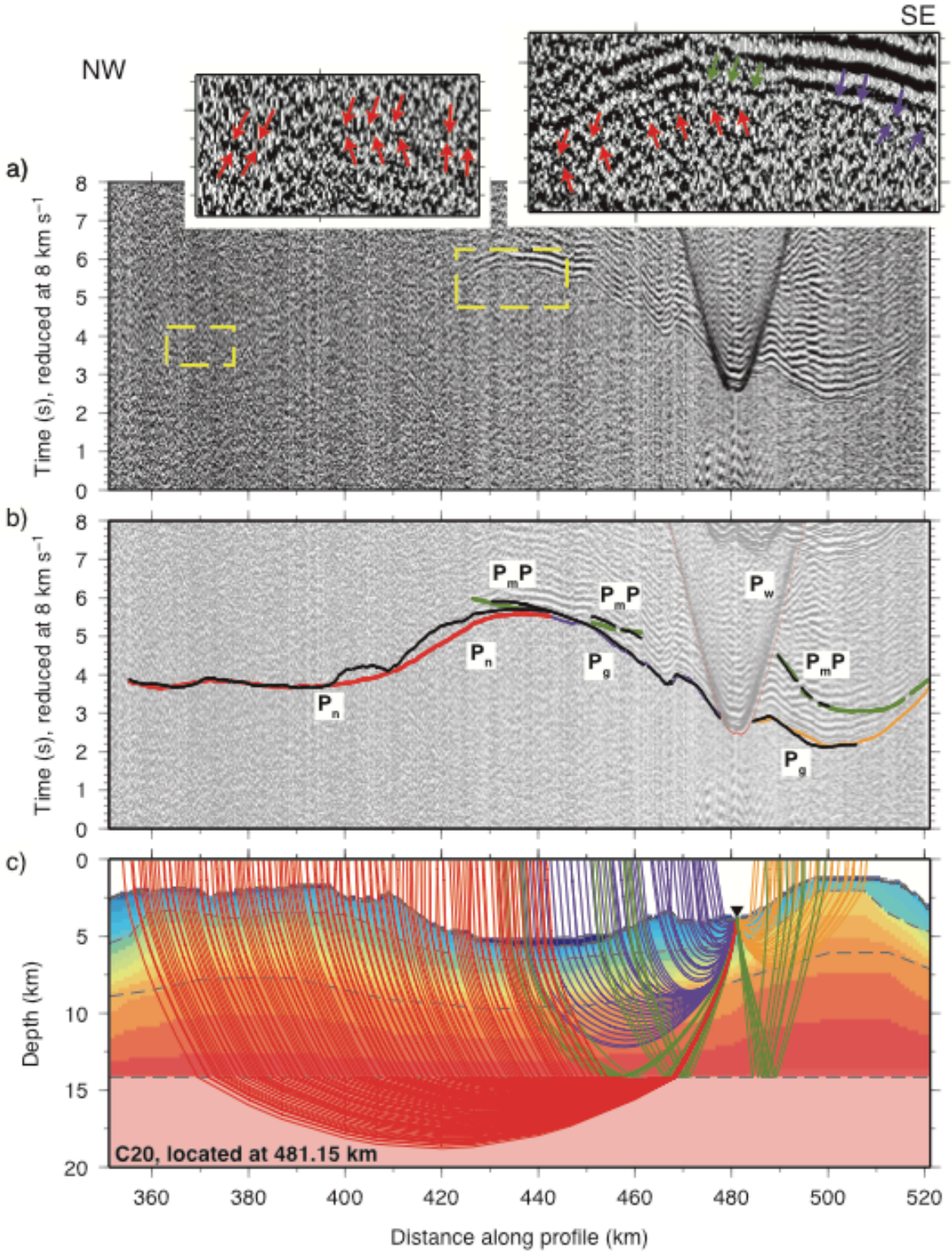

Figure 5: WA seismic data from OBS C20, located at 481.15 km d.a.p.. See Fig. 4 for details.

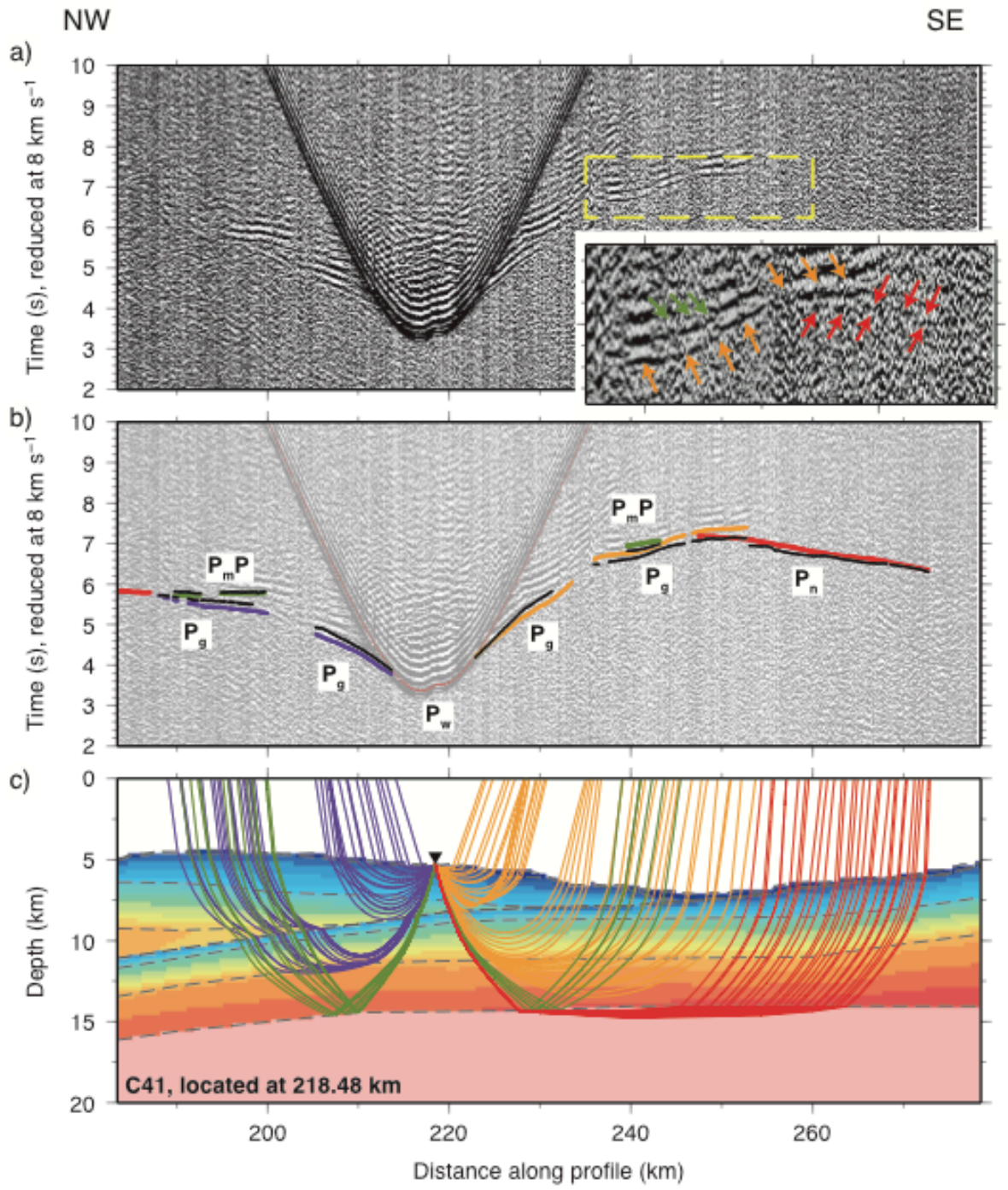

Figure 6: WA seismic data from OBS C41, located at 218.48 km d.a.p., on the Tonga lower forearc slope, adjacent to the Tonga trench. See Fig. 4 for details. Phases traced through both the overriding and subducting plates are not distinguished separately in the ray diagram.

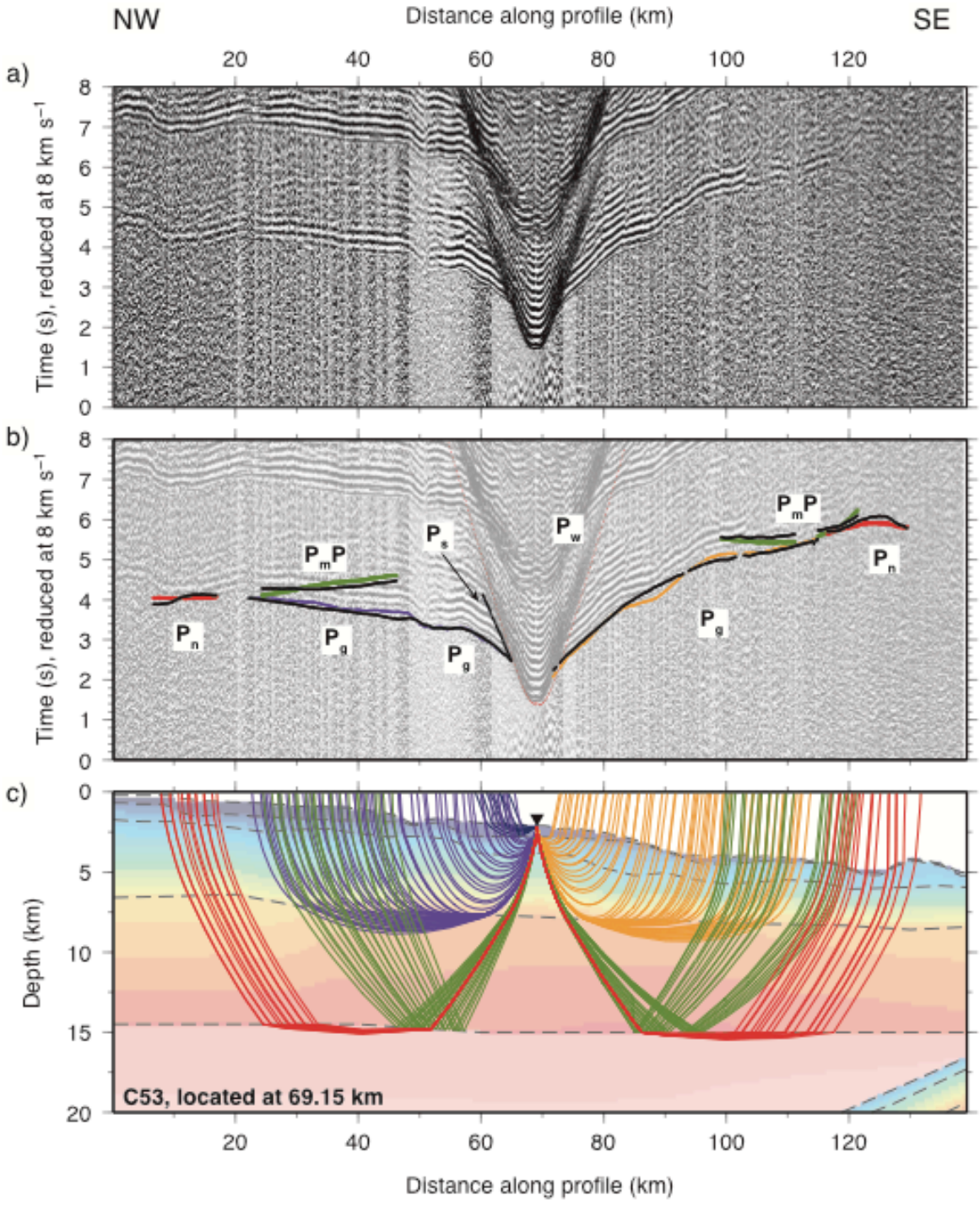

Figure 7: WA seismic data from OBS C53, located at 69.15 km d.a.p., on the Tonga upper forearc. See Fig. 4 for details.

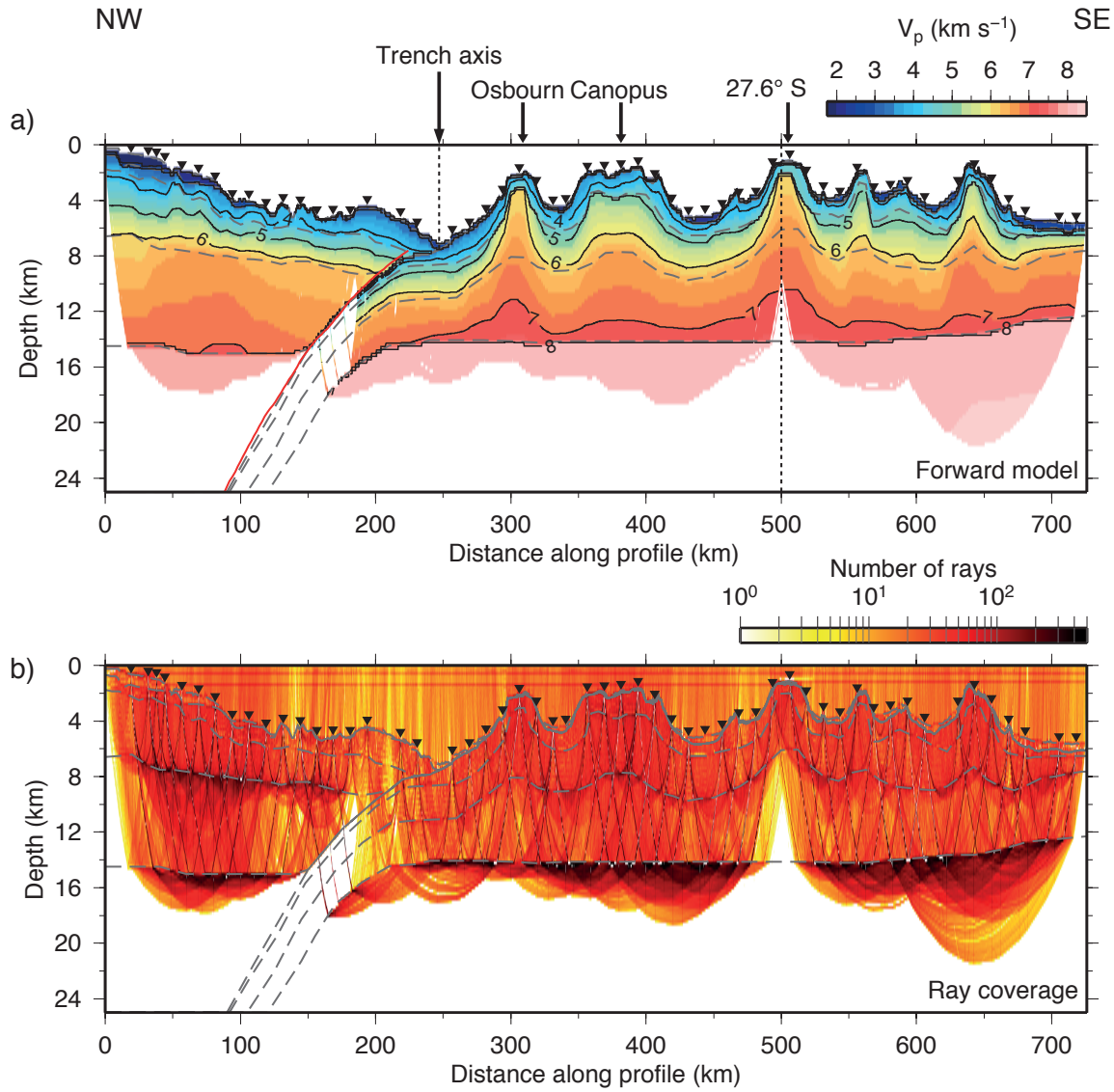

Figure 8: Best-fit WA forward model (a), masked to show only regions sampled by rays. Velocity contours are annotated at 1 km s^{-1} intervals. Solid red line represents the location of the subduction interface sampled from SLAB1.0 (Hayes et al. 2012). b) Ray coverage calculated in 0.2 x 0.2 km cells. Inverted black triangles indicate OBS locations along model. Dashed grey lines indicate the *rayinvr* crustal model layer boundaries.

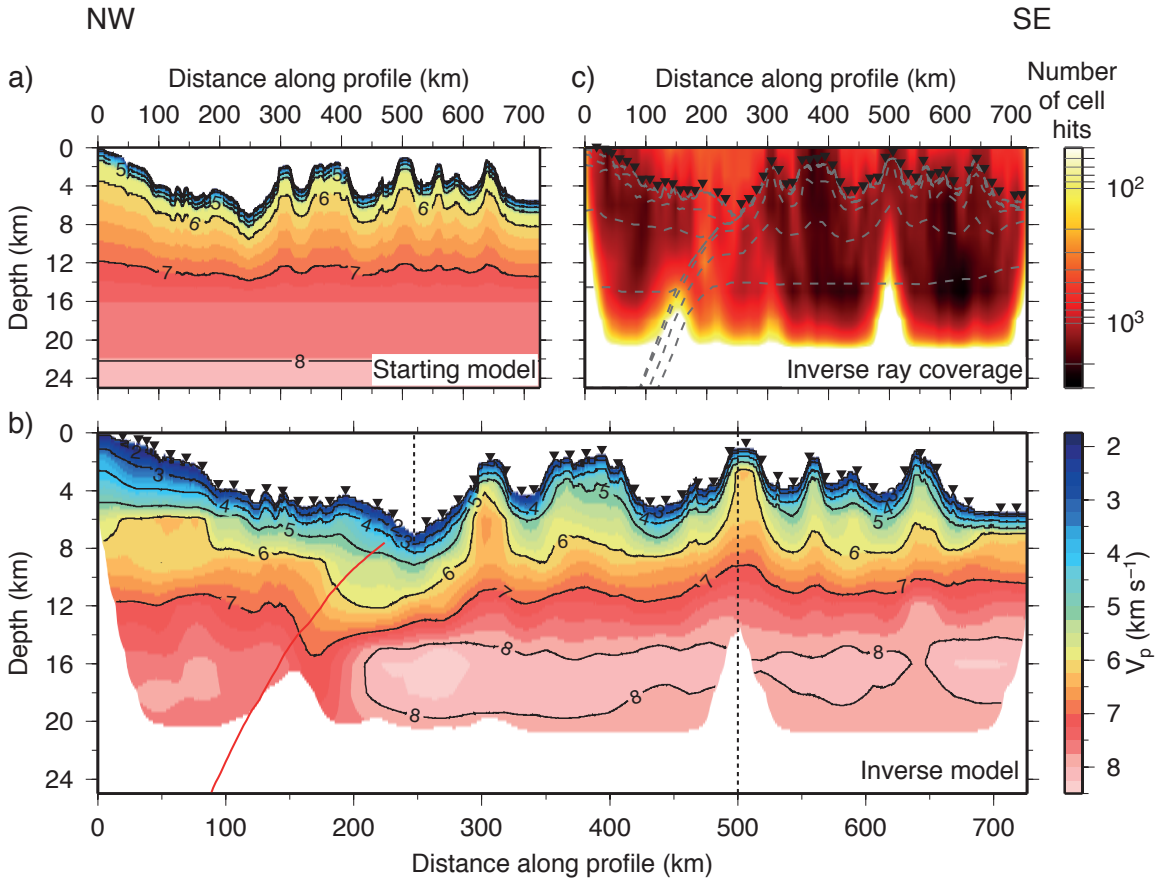

Figure 9: Assessment of model uniqueness by WA inverse modelling. a) Starting model for inversion, with 0.2 x 0.2 km forward node spacing. Velocity contours are drawn and annotated at 1 km s^{-1} intervals. b) Cell hit count at end of inversion. Dashed grey lines are *forward model* layer boundaries for comparison with Fig. 8b. c) Final inversion result after eight iterations at 8 x 3 km inverse cell size and five iterations at 4 x 2 km inverse cell size, producing a model with T_{rms} = 129 ms, χ^2 = 2.42. Output model is masked using the cell hit count in b) to show only regions sampled by rays. Contours as in a). Inverted black triangles indicate OBS locations along model. Solid red line represents the location of the subduction interface sampled from SLAB1.0 (Hayes et al. 2012).

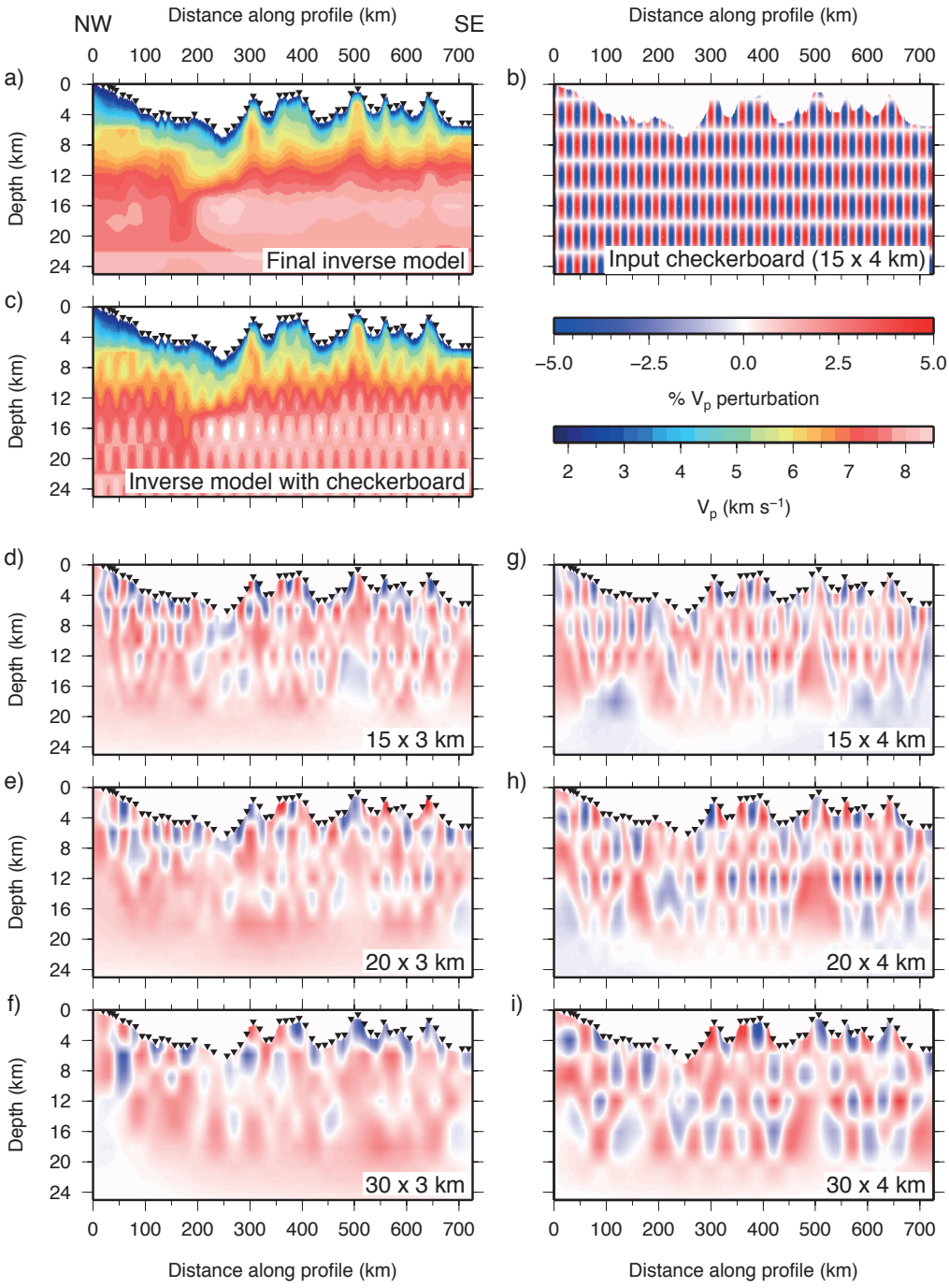

Figure 10: Results of *inverse model* resolution testing. a) Final *inverse model*, used as the basis of resolution testing. b) Example input checkerboard anomaly pattern, with a ± 5% velocity perturbation, and input anomaly dimensions of 15 x 4 km (horizontal x vertical). c) Final *inverse model* with the 15 x 4 km input anomaly pattern applied. d) 15 x 3 km, e) 20 x 3 km, f) 30 x 3 km, g) 15 x 4 km, h) 20 x 4 km, and i) 30 x 4 km recovered checkerboards. Good checkerboard recovery is achieved throughout the crust and into the upper mantle in g-i), except where ray coverage is limited, and in limited regions at shallow depths in d-e).

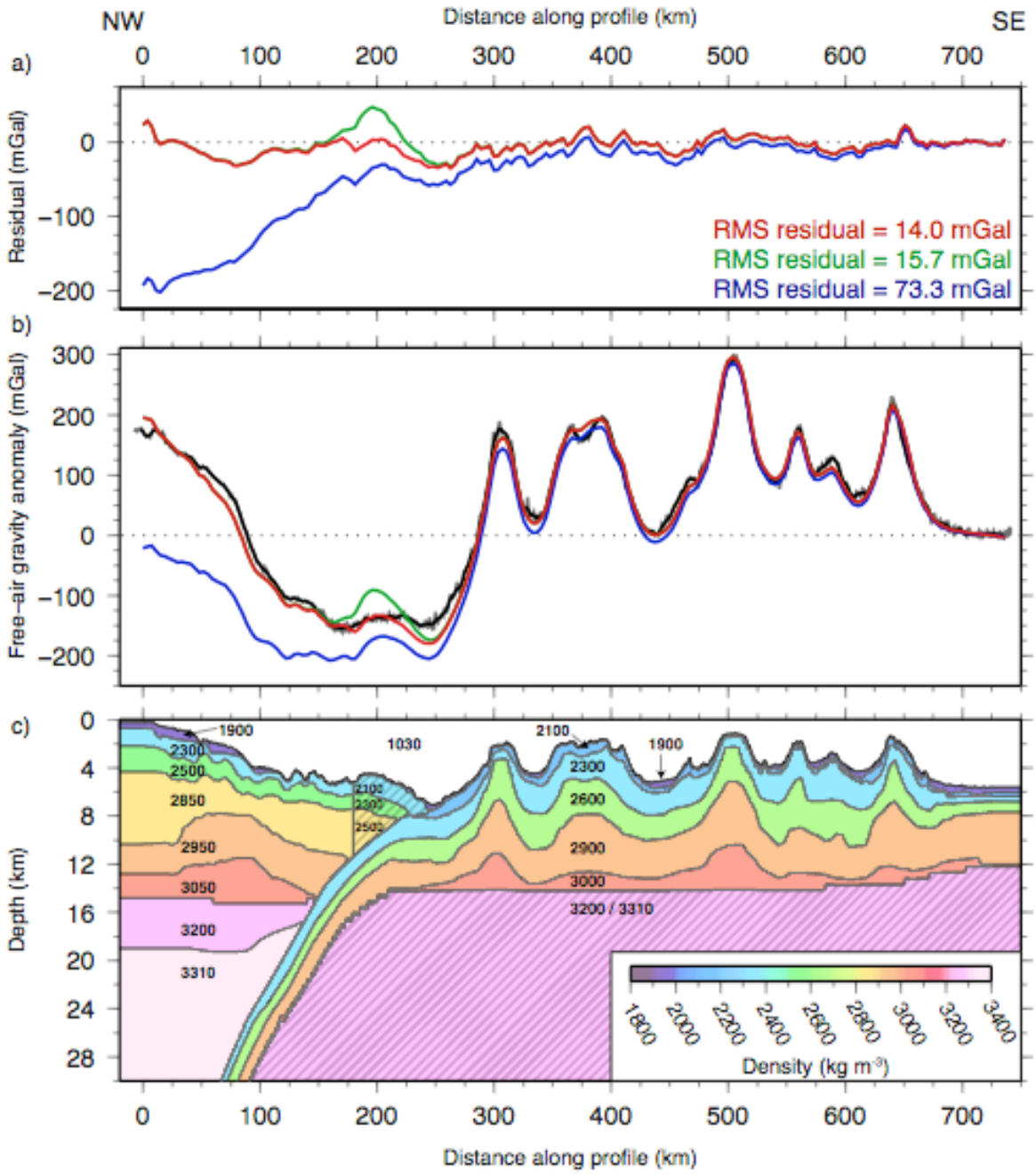

Figure 11: Assessment of model uniqueness using gravity modelling. Three different models are defined: red = best-fit *density model*, using lower quoted overriding upper-middle crust density values between 180 km d.a.p. and trench axis in c); green = model with constant overriding plate upper-middle crust density values; blue = model with same mantle density beneath both plates (3310 kg m^{-3}). Grey line = raw observed shipboard gravity. Black line = filtered observed shipboard gravity. a) RMS residual between observed and calculated FAA, coloured to match the corresponding density models described above. b) Calculated FAA coloured as in a). c) Density block models used to calculate the FAA, plotted to 30 km depth. Hatched regions indicate where the density is altered for each of the three different density models, with the alternative density values used indicated.

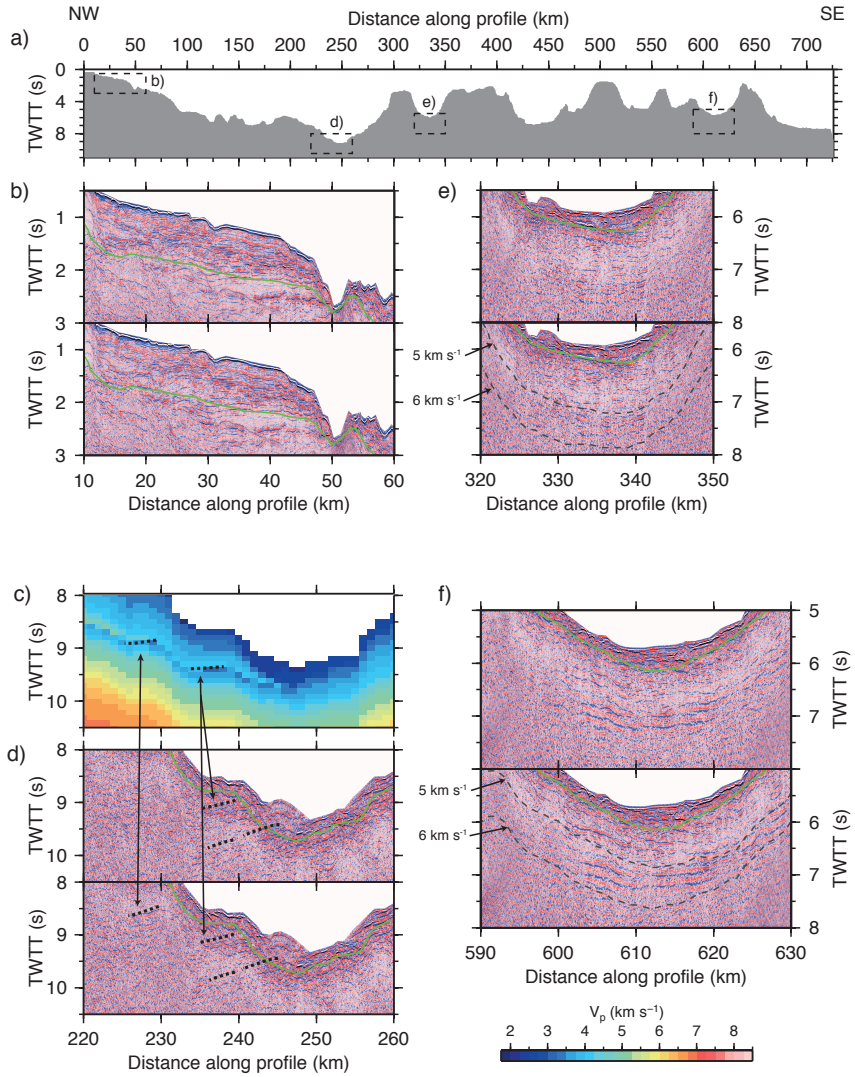

Figure 12: Profile C MCS data restacked using a stacking velocity-TWTT model derived from conversion of the best-fit WA *forward model* to TWTT and application of an inverse-Dix (1955) velocity conversion. Dashed boxes indicate areas covered by enlargements b-f). b) Upper Tonga forearc MCS reflection data stacked with (upper panel) single (1.5 km s^{-1}) and (lower panel) forward modelling-derived stacking velocities. Green line indicates the location of the *forward model* sediment-basement interface, converted to TWTT. c) WA forward velocity-TWTT model in the shallow plate boundary region (shown in d). d) Shallow plate boundary region displayed as for b) with upper (1.5 km s^{-1}) and lower (picked) stacking velocities. Dashed lines and arrows indicate locations of reflectivity which may be related to the TWTT manifestation of the plate boundary (cf. c). e) Saddle between Osbourn and Canopus seamounts, displayed as in b). Dashed grey lines indicate location of 5 and 6 km s^{-1} P-wave velocity contours, above which any sub-basement reflectivity associated with proposed explosive/extrusive magmatic products is observed. f) as for e) between two small seamounts at southern end of Profile C.

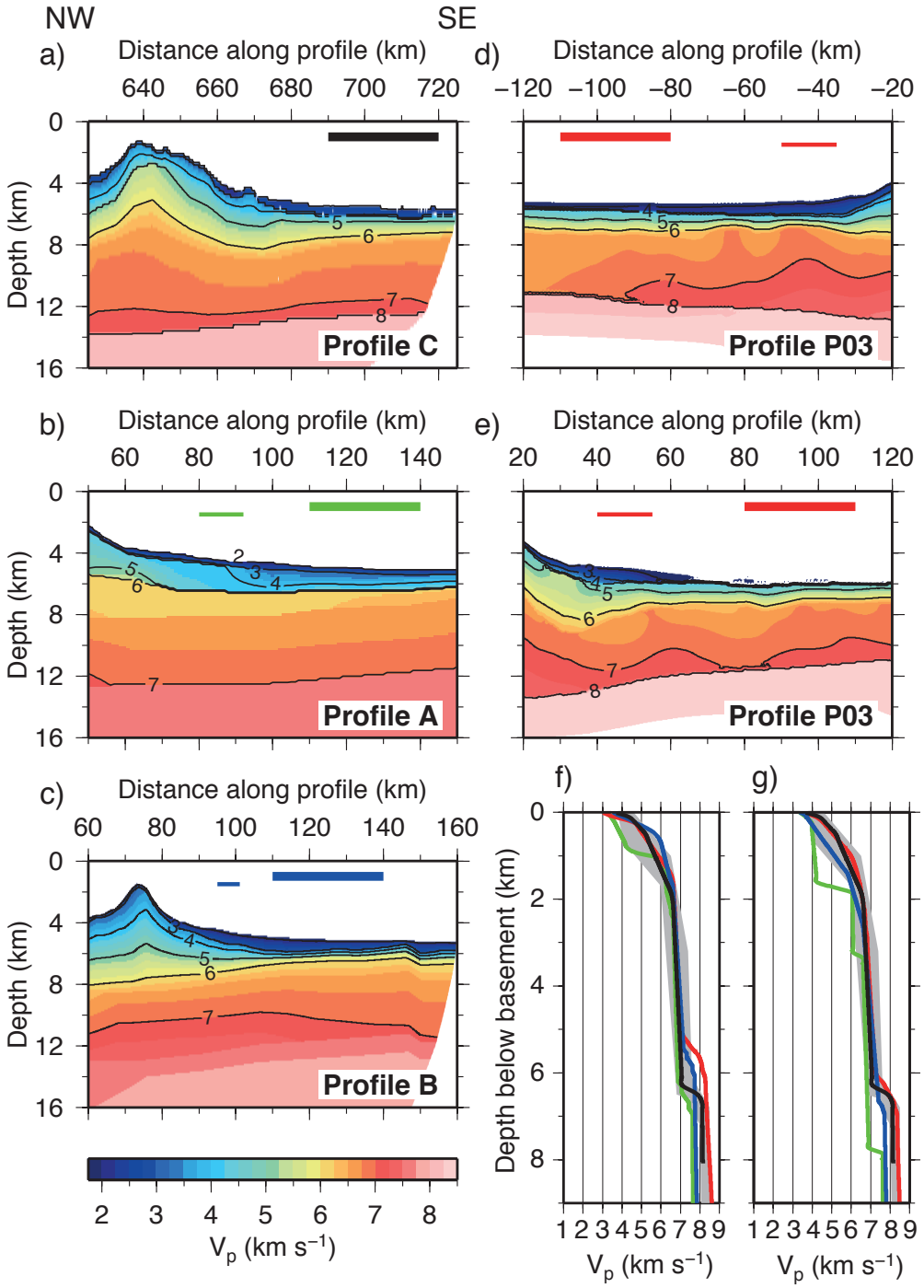

Figure 13: Best-fit P-wave velocity-depth models for oceanic crust adjacent to seamount edifices. a) Profile C, b) Profile A, and c) Profile B, and SO195 Profile P03 to the d) south and e) north of 27.6°S seamount. Horizontal coloured bars represent the ranges over which 1D profiles have been sampled and averaged. f) 1D velocity-depth profiles plotted as depth below basement for the models in a)-e) with colours matching thick bars in a)-e). g) 1D velocity-depth profiles sampled closer to seamount flanks at the locations indicated by thin coloured bars in a)-e). The White et al. (1992) average oceanic crustal structure is plotted as a grey envelope for reference.

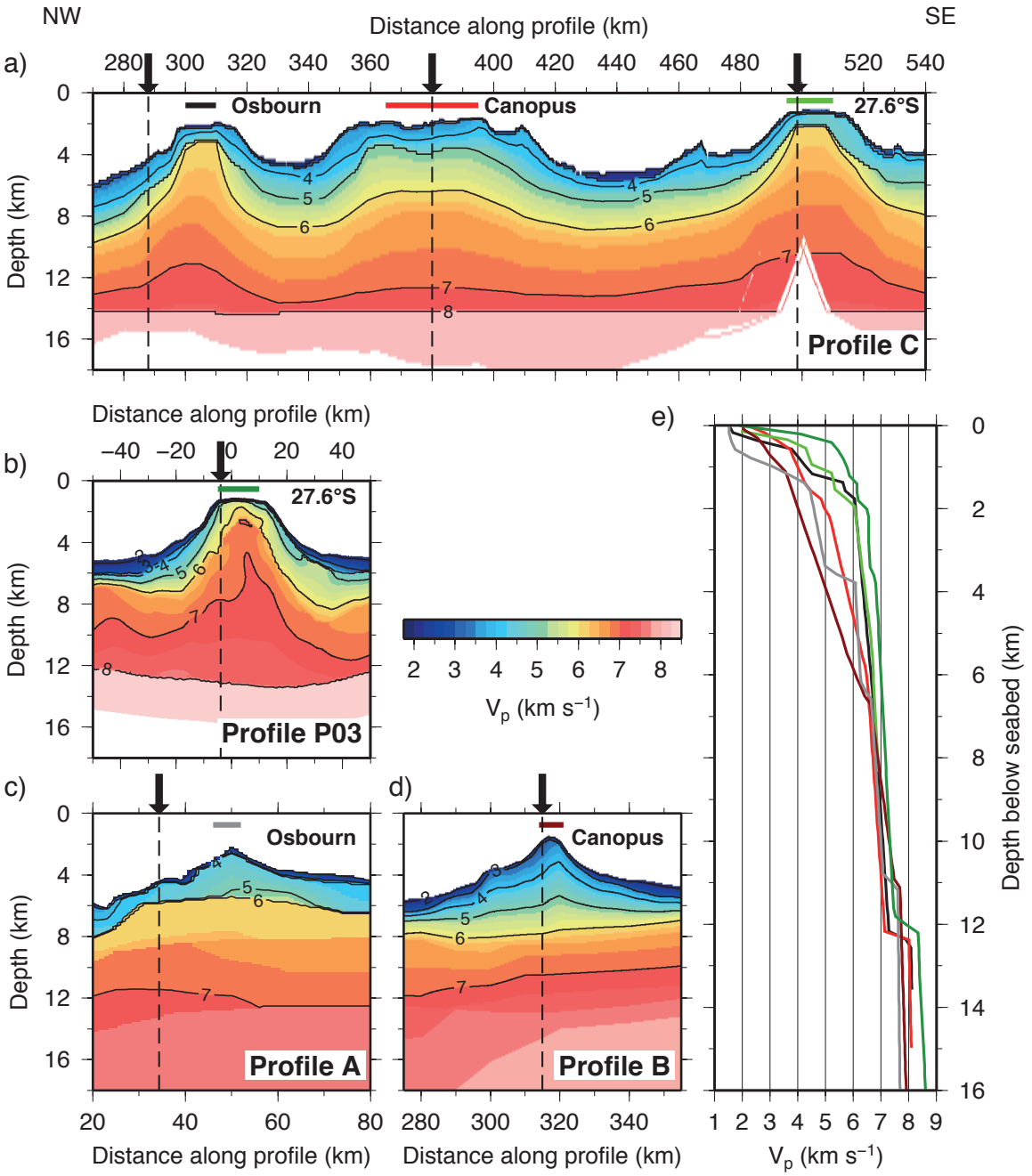

Figure 14: Best-fit P-wave velocity-depth models for large LRSC seamounts. a) Profile C velocity-depth *forward model* for Osbourn, Canopus and 27.6°S seamounts. b) Contreras-Reyes et al. (2010) model for 27.6°S seamount, where Profile P03 is orientated sub-perpendicular to Profile C. c) Stratford et al. (2015) model through the trench-ward flank of Osbourn seamount, where Profile A is oblique to Profile C. d) Funnell et al. (2017) model through Canopus seamount, where Profile B is orientated perpendicular to Profile C. Profile crossing locations are indicated by black arrows and dashed lines. In all panels, coloured bars indicate the location of averaged velocity-depth profiles shown in e). e) Averaged 1D velocity-depth profiles through seamounts in a)-d) with colours indicating sampling locations.

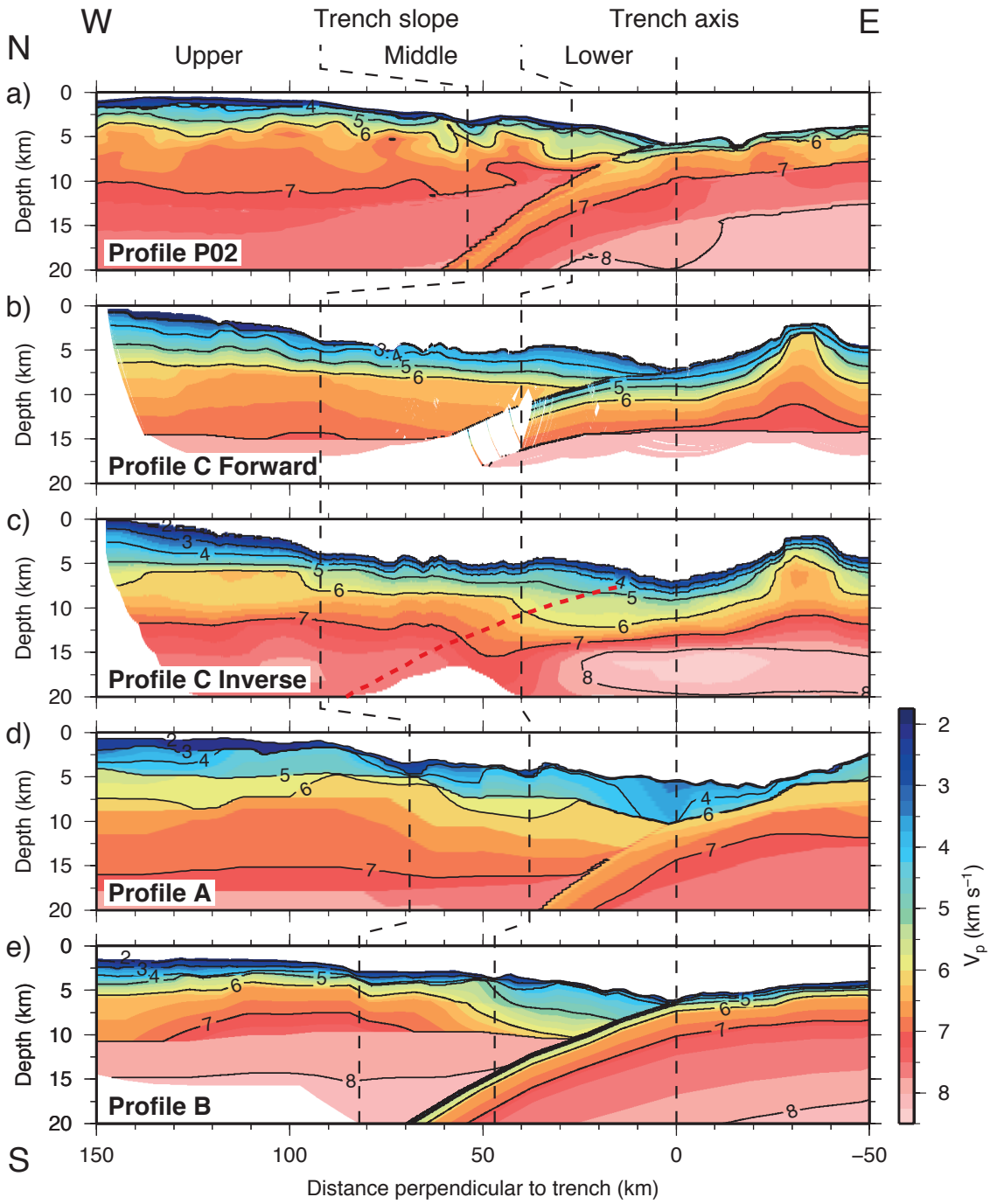

Figure 15: P-wave velocity-depth models crossing Tonga-Kermadec forearc and trench from Profiles a) P02 (Contreras-Reyes et al. 2011), b) C (*forward model*, this study), c) C (*inverse model*, this study), where the red dashed line indicates the location of the plate boundary, d) A (Stratford et al. 2015), and e) B (Funnell et al. 2017). Profiles have been projected perpendicular to the trench and aligned relative to the trench axis, and are ordered from north to south in terms of their trench-crossing location. Dashed black lines show the along-margin variability in trench-slope morphology.